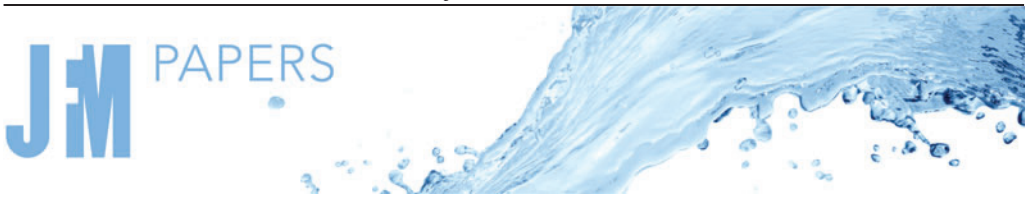
CrossMark

J. Fluid Mech. (2022), *vol*. 947, A2, doi:10.1017/jfm.2022.606



Exact coherent states in plane Couette flow under spanwise wall oscillation

Yacine Bengana[1],†, Qiang Yang[2], Guohua Tu[2],† and Yongyun Hwang[1]

[1]Department of Aeronautics, Imperial College London, South Kensington, London SW7 2AZ, UK

[2]State Key Laboratory of Aerodynamics, China Aerodynamics Research and Development Centre, Mianyang 621000, PR China

(Received 1 March 2022; revised 13 June 2022; accepted 27 June 2022)

A set of several exact coherent states in plane Couette flow is computed under spanwise wall oscillation control, with a range of wall oscillation amplitudes and periods (A_w, T). It is found that the wall oscillation generally stabilises the upper branch of the equilibrium solutions and achieves the corresponding drag reduction, while it influences modestly the lower branch. The stabilisation effect is found to increase with the oscillation amplitude with an optimal time period around $T^+ \approx 100$. The exact coherent states reproduce some key dynamical behaviours of streaks observed in previous studies, while exhibiting the rich coherent structure dynamics that cannot be extracted from a phase average of turbulent states. Visualisation of state portraits shows that the size of the state space supporting turbulent solution is reduced by the spanwise wall oscillation, and the upper-branch equilibrium solutions become less repelling, with many of their unstable manifolds being stabilised. This change of the state space dynamics leads to a significant reduction in lifetime of turbulence. Finally, the main stabilisation mechanism of the exact coherent states is found to be the suppression of the lift-up effect of streaks, explaining why previous linear analyses have been so successful for turbulence stabilisation modelling and the resulting drag reduction.

Key words: flow control, turbulent flows, nonlinear dynamical systems

1. Introduction

Turbulent skin-friction drag in wall-bounded shear flows is a main concern for many engineering applications, and it is closely associated with the turbulence regeneration mechanism in the vicinity of the wall. This mechanism, known as the self-sustaining process (Hamilton, Kim & Waleffe 1995; Waleffe 1997), involves quasi-streamwise vortices and low- and high-speed streaks of streamwise velocity. The streaks are formed

† Email addresses for correspondence: y.bengana14@imperial.ac.uk, ghtu@skla.cardc.cn

© The Author(s), 2022. Published by Cambridge University Press

https://doi.org/10.1017/jfm.2022.606 Published online by Cambridge University Press

from the quasi-streamwise vortices via the lift-up mechanism (e.g. Ellingsen & Palm 1975; Landahl 1980; Gustavsson 1991; Butler & Farrell 1993; Chernyshenko & Baig 2005; del Álamo & Jiménez 2006; Pujals *et al.* 2009; Hwang & Cossu 2010; McKeon & Sharma 2010; Brandt 2014) and experience successively an instability or a transient growth (Hamilton *et al.* 1995; Schoppa & Hussain 2002; Cassinelli, de Giovanetti & Hwang 2017), leading to their breakdown. Finally, the cycle starts with the generation of new quasi-streamwise vortices. During the self-sustaining process, the quasi-streamwise vortices bring high streamwise momentum to the wall as part of the lift-up mechanism, and generate the high-speed streaks, while they also pump near-wall fluids with low streamwise momentum away from the wall, generating the low-speed streaks. In the near-wall region of turbulent flow, the former effect is more important than the latter. As such, the downwash of the flow led by the quasi-streamwise vortices has been understood to be responsible for a large portion of skin-friction generation, at least at low Reynolds numbers (Kravchenko, Choi & Moin 1993).

Various approaches have been proposed for the reduction of the skin-friction drag generated by the near-wall turbulence (see also a review by Leschziner, Choi & Choi 2011), such as the spanwise wall oscillation (Jung, Mangiavacchi & Akhavan 1992), riblets (Walsh 1983; Choi 1989; Choi, Moin & Kim 1993; García-Mayoral & Jiménez 2011), blowing and suction (Choi, Moin & Kim 1994), travelling waves (Karniadakis & Choi 2003), body forcing (Schoppa & Hussain 1998; Xu *et al.* 2007; Willis, Hwang & Cossu 2010; Yao, Chen & Hussain 2018), superhydrophobic surface (e.g. Lee, Jelly & Zaki 2015), baffles (Hof *et al.* 2010; Kühnen *et al.* 2018; Marensi, Willis & Kerswell 2019; Marensi *et al.* 2020), and many others. Among them, the spanwise wall oscillation can attain a drag reduction as high as 40 % at relatively low Reynolds numbers. The skin-friction drag decreases monotonically with the wall oscillation amplitude until a plateau above some critical value (Quadrio & Ricco 2004; Quadrio, Ricco & Viotti 2009). For a given oscillation amplitude, the optimal drag reduction for fully developed turbulent flow is attained at the optimal time period of oscillation $T^+ \approx 100$ (scaled in viscous inner units) (Jung *et al.* 1992). The drag reduction effect has been validated both numerically (Baron & Quadrio 1995; Quadrio & Sibilla 2000; Lardeau & Leschziner 2013) and experimentally (Choi, Debisschop & Clayton 1998; Choi & Graham 1998; Auteri *et al.* 2010; Choi, Jukes & Whalley 2011; Gatti *et al.* 2015; Bird, Santer & Morrison 2018), and the emerging evidence suggests that there is an important Reynolds number effect (Touber & Leschziner 2012; Chung, Hurst & Yang 2013; Gatti & Quadrio 2013; Agostini, Touber & Leschziner 2014; Hurst, Yang & Chung 2014; Agostini & Leschziner 2021; Marusic *et al.* 2021). The time-harmonic spanwise wall oscillation can also be extended to a spatial form, i.e. a streamwise stationary wave (Viotti, Quadrio & Luchini 2009; Skote 2013), and to a spatio-temporal form, i.e. a streamwise travelling wave (Quadrio *et al.* 2009).

The spanwise wall motion generates a layer (i.e. the Stokes layer) in which the spanwise viscous effect due to the wall motion remains important. The Stokes layer can interact with the near-wall coherent structures, resulting in a significant amount of drag reduction (Touber & Leschziner 2012; Chung *et al.* 2013; Yang 2016). Choi, Xu & Sung (2002) proposed an empirical parameter that relates the effect of the oscillating Stokes layer to the amount of drag reduction. This parameter was later improved further by Quadrio & Ricco (2004) and Ricco & Quadrio (2008) based on a large direct numerical simulation (DNS) database for the spanwise wall oscillation. The turbulent kinetic energy and enstrophy balances have also been well studied in the presence of spanwise wall oscillation. The analysis of Xu & Huang (2005) for the Reynolds stress budget during the first two wall oscillation periods showed that there is a sustained attenuation of the pressure-strain term,

https://doi.org/10.1017/jfm.2022.606 Published online by Cambridge University Press

which was proposed to be the mechanism of the global attenuation of turbulence. Ricco *et al.* (2012) suggested that an initial enstrophy increase is an important process that results in the drag reduction. However, Agostini *et al.* (2014) pointed out that the drag reduction process is more linked to the rate of change in the Stokes strain (the wall-normal gradient of the spanwise velocity), rather than the enstrophy itself. Several reviews on these issues are available along the historical development (Karniadakis & Choi 2003; Quadrio 2011; Leschziner 2020; Ricco, Skote & Leschziner 2021), and the reader may refer to them.

A common observation in the near-wall turbulence subject to the spanwise wall oscillation is that the development of streaks appears to be highly affected by the oscillation. In the context of the linear analysis of the Navier–Stokes equations, Duque-Daza *et al.* (2012) observed that there is a good correlation between the amount of drag reduction and the change of the streak amplification in the Stokes layer. The time-dependent streak angle relative to the downstream direction is another feature observed in the presence of the spanwise wall oscillation control (Jung *et al.* 1992; Sendstad 1992; Choi *et al.* 1998; Quadrio & Sibilla 2000; Ricco 2004; Touber & Leschziner 2012; Chung *et al.* 2013; Yakeno, Hasegawa & Kasagi 2014; Yang 2016). The streak angle was found to vary slowly with time for half an oscillation period, then jump suddenly to another value, changing both the sign and the magnitude. Such a behaviour has been related to the dynamic variation of the turbulent statistics, as was investigated thoroughly by Touber & Leschziner (2012) and Agostini *et al.* (2014). Blesbois *et al.* (2013) refined the work of Duque-Daza *et al.* (2012) by applying the optimal perturbation framework of Chernyshenko & Baig (2005), and made more quantitative predictions for the streak pattern. In particular, their linear analysis revealed that there is a short time interval in the oscillation period during which the optimal perturbation resulting in the streaks with a certain angle grows strongly, and this angle remains dominant for almost half of the entire wall oscillation period, consistent with the observation from DNS. In a similar context, Hicks & Ricco (2015) examined the evolution of streaks driven by a free-stream noise in a laminar boundary layer. They found that the energy of laminar streaks can be reduced by 90 % due to the spanwise wall oscillation. The modal and non-modal instability of a boundary layer subject to the spanwise wall oscillation was also investigated by Hack & Zaki (2015), who found that the spanwise wall oscillation weakens the non-modal growth, while the modal instability is promoted at high wall oscillation amplitudes.

From the viewpoint of dynamical systems, turbulence is viewed as a time-dependent chaotic solution trajectory in a high-dimensional state space. Invariant solutions of the given dynamical system, such as equilibria, travelling waves and (relative) periodic orbits, are the crucial elements that characterise the chaotic trajectory of turbulence, and numerous solutions have been discovered in plane Couette flow (Nagata 1990; Waleffe 1998, 2003; Kawahara & Kida 2001; Gibson, Halcrow & Cvitanovic 2008, 2009; Eckhardt & Zammert 2018; Reetz, Kreilos & Schneider 2019), plane Poiseuille flow (Waleffe 2001; Viswanath 2007; Nagata & Deguchi 2013; Park & Graham 2015; Hwang, Willis & Cossu 2016; Yang, Willis & Hwang 2019), pipe flow (Faisst & Eckhardt 2003; Wedin & Kerswell 2004; Duguet, Willis & Kerswell 2008; Willis, Cvitanović & Avila 2013; Budanur *et al.* 2017), stress-driven shear flows (Doohan, Willis & Hwang 2019; Doohan *et al.* 2021) and boundary layers (Khapko *et al.* 2013; Kreilos, Gibson & Schneider 2016*a*; Kreilos *et al.* 2016*b*). Many of the invariant solutions found are composed of low- and high-speed streaks and quasi-streamwise vortices similar to the structures in near-wall turbulence. In this sense, they have often been referred to as exact coherent states (ECS) (Waleffe 2001). Some reviews are available on the physical significance of the invariant solutions from the

https://doi.org/10.1017/jfm.2022.606 Published online by Cambridge University Press

dynamical systems view of transition and turbulence (Kerswell 2005; Eckhardt *et al.* 2007; Kawahara, Uhlmann & van Veen 2012; Graham & Floryan 2021).

An extensive body of work investigates transition to turbulence within the dynamical systems framework. Wall-bounded shear flows at typical transitional Reynolds numbers do not exhibit any linear instability: for example, laminar basic states of pipe flow (Lessen, Sadler & Liu 1968) and plane Couette flow (Romanov 1973) are linearly stable for all Reynolds numbers. In such flows, a pair of invariant solutions typically first emerges as a precursor of turbulence, while breaking the global stability of the laminar basic state. The solution with high skin-friction drag is often referred to as the 'upper-branch' solution, and the other with low drag is the 'lower-branch' solution. As the Reynolds number is increased, the upper-branch solution experiences a bifurcation cascade towards turbulence (or chaos). On the contrary, the lower-branch solution often sits on a high-dimensional state space surface that separates the laminar and turbulent states. This surface is referred to as the 'edge', and the lower-branch solution often plays a key role in characterising the attractor on the edge, i.e. the 'edge state' (Skufca, Yorke & Eckhardt 2006). The turbulent state, evolved from the upper-branch solution, can collide with the edge if the Reynolds number is sufficiently high, allowing it to be relaminarised (Kreilos & Eckhardt 2012; Lustro *et al.* 2019). Subsequently, the turbulence becomes transient in time featured with a finite lifetime, although the lifetime increases quickly with the Reynolds number.

Understanding the state space dynamics can also be useful for flow control, as it offers a different perspective on the given problem of interest: for example, the state space feature discussed above was utilised for the purpose of flow control by Kawahara (2005), who demonstrated relaminarisation of turbulent Couette flow by applying a spanwise rotation when the solution trajectory reaches the edge of turbulence. In general, under a constant action of passive or active control, the state space dynamics is expected to be deformed in a systematic manner, and the understanding of this deformation may be useful for further development of the given control strategy. For this purpose, several previous studies have investigated how invariant solutions, which form the skeleton of the state space dynamics, are changed by the given control mechanism: for example, polymer solution (Stone, Waleffe & Graham 2002; Stone *et al.* 2004; Li, Xi & Graham 2006; Li & Graham 2007), blowing and suction (Ibrahim *et al.* 2019), slip boundary condition (Davis & Park 2020) and stratification (Langham, Eaves & Kerswell 2020). As for the spanwise wall oscillation, a preliminary investigation was performed by two of the authors of the present study (Yang & Hwang 2019) using a pair of the inner-scaled wall-attached travelling wave solutions identified by Yang *et al.* (2019) in plane Poiseuille flow. Although this previous work showed that the spanwise wall oscillation leads these solutions to emerge at higher Reynolds numbers, the full state space dynamics has not been understood yet: for example, it was observed previously that the spanwise wall oscillation might drive turbulence to a lower-branch solution (Kushwaha 2017). Finally, from this perspective, it is worth mentioning the recent work by Rabin, Caulfield & Kerswell (2014), who demonstrated that the oscillating wall leads to a more stable laminar state by increasing the critical energy of the 'optimal seed' for the onset of turbulence (i.e. nonlinear optimal perturbation) by 41 %. This observation suggests that the spanwise wall motion yields a non-trivial change not only around the laminar basic state but also in the entire state space.

The objective of the present study is to characterise the state space dynamics of near-wall turbulence under spanwise wall oscillation, thereby taking a step towards the nonlinear regime from the previous linear analyses. To this end, we consider several invariant solutions found previously in plane Couette flow (Nagata 1990; Gibson *et al.* 2009) and assess their behaviour in the presence of spanwise wall oscillation. Given the

https://doi.org/10.1017/jfm.2022.606 Published online by Cambridge University Press

technical difficulty for the computation of periodic orbits with the unsteady wall motion, particular focus of the present study is given to equilibrium solutions. We will see that the spanwise wall oscillation stabilises most of the equilibrium solutions and sometimes even leads some of them to disappear through a saddle–node bifurcation. Furthermore, the equilibrium solutions organised around the turbulent state (i.e. upper-branch solutions) retrieve many features of the near-wall coherent structures observed in the previous DNS under the spanwise wall oscillation. Visualisation of some state portraits with key observables of interest suggests that the size of the state space supporting the turbulent state is reduced by the spanwise wall oscillation. Finally, the lifetime of turbulence is also found to be reduced significantly with the equilibrium solutions stabilised overall, suggesting that turbulence itself is stabilised due to the spanwise wall oscillation.

The paper is organised as follows. In § 2, we introduce the numerical methods for the spanwise wall oscillation control and the equilibrium solutions (the exact coherent states) search and continuation. The main results and discussion are presented in § 3, where we investigate the effect of the spanwise wall oscillation control on the exact coherent states from various aspects, including the bifurcation diagram, statistics, streak variation, state portrait, eigenspectra, turbulence lifetime and the self-sustaining process. Finally, the paper is concluded in § 4 with a summary of its key findings.

2. Problem formulation

We consider the three-dimensional incompressible plane Couette flow of Newtonian fluid with density ρ and kinematic viscosity ν (dynamic viscosity μ). In the present study, two computational domains are chosen from the well-known previous studies (i.e. Nagata 1990; Hamilton *et al.* 1995; Waleffe 2003), and they are referred to conveniently as Ω_N (Nagata 1990; Waleffe 2003) and Ω_{HKW} (Hamilton *et al.* 1995), respectively. The domain size and the grid numbers used are listed in table 1. Flows in these domains were studied extensively by Hamilton *et al.* (1995), Gibson *et al.* (2008, 2009) and many others. The streamwise, wall-normal and spanwise directions are denoted by x, y and z, respectively, and the corresponding velocity components by u, v and w. The flow is driven by moving the upper ($y = 2h$) and lower ($y = 0$) walls in opposite directions: i.e. $u|_{y=0} = -U_w$ and $u|_{y=2h} = U_w$, where U_w is the wall moving velocity in the streamwise direction. The Reynolds number is defined as $Re = U_w h/\nu$, where h is the half channel width. No-slip boundary conditions are applied to both the upper and lower walls. The numerical simulations are carried out using the Navier–Stokes solver Diablo (Bewley 2014). The wall-parallel directions (x and z) are discretised using Fourier series with the 2/3 dealiasing rule (Goodman, Hou & Tadmor 1994). The wall-normal direction is discretised using the second-order central difference. The time integration is carried out by combining the Crank–Nicolson method with a low-storage third-order Runge–Kutta method. This code has been validated extensively in previous studies (e.g. Hwang 2013; Hwang & Bengana 2016; Yang *et al.* 2019) as well as in Appendix A, where the mean velocity is compared with that in Kawahara & Kida (2001).

In the present study, the Reynolds number is chosen to be $Re = 400$, which gives $Re_\tau = 33.3$ and 33.9 for the two computational domains Ω_N and Ω_{HKW}, respectively (see also table 2). This choice is made to study the dynamics of near-wall coherent structure primarily, such that the computational domain becomes the well-known minimal flow unit (Jiménez & Moin 1991; Hamilton *et al.* 1995): for example, the inner-scaled domain size of Ω_{HKW} is $(L_x^+, L_y^+, L_z^+) = (186, 67.8, 133)$, just large enough to study the dynamics of a single pair of low/high-speed streaks and the related quasi-streamwise vortices.

https://doi.org/10.1017/jfm.2022.606 Published online by Cambridge University Press

Domain	L_x/h	L_y/h	L_z/h	N_x	N_y	N_z	Equilibria
Ω_N	3.4662π	2	1.7391π	32	61	32	EQ0
Ω_{HKW}	1.75π	2	1.2π	32	61	64	EQ1, EQ4, EQ7, PO

Table 1. Domain sizes and grid numbers of the flow configuration used in the present study. Four pairs of equilibria are considered in total, i.e. one in Ω_N and four (including an edge state, PO) in Ω_{HKW}.

State	Domain	Re	Re_τ	A_w/U_w	TU_w/h	A_w^+	T^+
DNS	Ω_N	400	33.3	0	—	0	—
EQ0	Ω_N	400	—	0–1.2	1–150	0–14.4	2.8–415.8
DNS	Ω_{HKW}	400	33.9; 32.5; 31.9	0; 0.4; 1.5	—; 10; 5	0; 4.7; 17.7	—; 28.7; 14.3
EQ1	Ω_{HKW}	400	—	0–3.0	1–50	0–35.4	2.9–143.3
EQ4	Ω_{HKW}	400	—	0–1.8	1–10	0–21.2	2.9–28.7
EQ7	Ω_{HKW}	400	—	0–2.0	1–50	0–23.6	2.9–143.3

Table 2. Control parameters for the studied cases. The superscript + indicates normalisation by viscous inner units of the corresponding uncontrolled DNS of each computational domain. Cases A and B studied in § 3 are EQ0 with $Re = 400$, $T^+ = 166.4$, $A_w^+ = 2.6$ and 4.4, respectively. The semicolons referring to the DNS in Ω_{HKW} separate the uncontrolled and controlled cases.

With this choice, the dynamical systems approach involving the computation of equilibrium solutions and unstable periodic orbits becomes a useful tool to study the turbulence dynamics. In this respect, it should be mentioned that the understanding to be gained from this study would be limited precisely to the near-wall coherent structure dynamics, which has been understood to be largely independent of the outer flow (Jiménez & Pinelli 1999; Hwang 2013).

2.1. *Spanwise wall oscillation control*

The spanwise wall oscillation applies the following control law to the walls:

$$W_w(t) = A_w \sin(2\pi t/T), \tag{2.1}$$

where $W_w(t)$ is the spanwise velocity at the walls, A_w is the amplitude of the spanwise wall velocity, T is the wall oscillation period, and t is the time. In this study, the upper and lower walls are set to oscillate in phase in the spanwise direction, i.e. $W_w(t)|_{y=0} = W_w(t)|_{y=2h}$. The control is applied to a set of equilibrium solutions and DNS by varying A_w and T, as summarised in table 2. The parameters are also scaled by viscous inner units of the uncontrolled DNS in the corresponding computational domain, so that $A_w^+ = A_w/u_\tau$ and $T^+ = T{u_\tau}^2/\nu$, where $u_\tau = \sqrt{\tau_w/\rho}$ is the skin-friction velocity with $\tau_w = \mu\langle\overline{\partial u/\partial y}|_{y=0,2h}\rangle_{x,z}$ being the streamwise wall shear stress of the uncontrolled DNS at $Re = 400$ unless stated otherwise. Here, $\langle\cdot\rangle_{x,z}$ indicates the average in streamwise and spanwise directions, and $\overline{(\cdot)}$ indicates the time average. The skin-friction coefficient is defined as $C_f = 2\tau_w/(\rho {U_w}^2) = 2(Re_\tau/Re)^2$, where $Re_\tau = u_\tau h/\nu$ is the friction Reynolds number. The spanwise wall oscillation control has been implemented and verified in our previous study for plane Poiseuille flow (Yang & Hwang 2019) by comparing with the DNS data of Hurst *et al.* (2014). Following previous studies (e.g. Hurst *et al.* 2014), we define the drag reduction rate $\mathcal{DR}$ as the relative change in the C_f values between the

https://doi.org/10.1017/jfm.2022.606 Published online by Cambridge University Press

controlled and uncontrolled states, i.e.

$$\mathcal{DR}\,(\%) = \frac{C_{f,0} - C_f}{C_{f,0}}, \tag{2.2}$$

where $C_{f,0}$ is the skin-friction coefficient of the uncontrolled state.

2.2. *Computation of equilibrium solutions and edge states*

In this study, we consider four pairs of equilibrium states (lower- and upper-branch solutions): EQ0 in Ω_N (Nagata 1990) and EQ1, EQ4, EQ7 in Ω_{HKW} (Gibson *et al.* 2008), which are listed in table 1. As discussed in § 1, the lower branch of the solutions has low drag and has been associated with the dynamics of the 'edge', the laminar-turbulent state space separatrix, while the upper branch is characterised with high drag and exhibits many features of turbulent state – note that the term 'branch' implies each member of a solution pair. The equilibrium states are computed using the Newton–Krylov–Hookstep method (Viswanath 2007; Willis *et al.* 2013). The algorithm finds the equilibrium states by zeroing numerically the relative error between the initial condition and the following final solution translated in time and space at $t = T_0$:

$$r = \frac{\|\sigma\,(-s_x, -s_z)\,\Phi^{T_0}(\boldsymbol{u}) - \boldsymbol{u}\|}{\|\boldsymbol{u}\|}, \tag{2.3}$$

where $\boldsymbol{u}$ is the initial state, $\Phi^{T_0}(\boldsymbol{u})$ is the state at $t = T_0$ with the state transition operator $\Phi^t(\cdot)$, and r is the relative error. Here $\sigma\,(-s_x, -s_z)$ is the spatial shift operator representing a translation by distance s_x in the streamwise direction and s_z in the spanwise direction, i.e. $\sigma\,(-s_x, -s_z)\,\boldsymbol{u}(x, y, z) = \boldsymbol{u}(x - s_x, y, z - s_z)$. In the present study, the relative error $r < 10^{-8}$ is chosen for all the solutions, which gives good numerical convergence. The equilibrium solutions from Gibson *et al.* (2008) (http://channelflow.org/dokuwiki/doku.php?id=database) were taken as the starting point for our Newton iteration. The period T_0 can be fixed arbitrarily for uncontrolled cases as the equilibrium states in this study are time-independent, and $T_0 = 8h/U_w$ is chosen. However, under the spanwise wall oscillation, the flow shows a periodicity due to the presence of periodic wall motion, thus the time interval needs to satisfy $T_0 = nT$, where T is the spanwise wall oscillation period, and n is a positive integer number. In general, there is no reason for T_0 and T to be identical (i.e. $n = 1$), as they are different quantities – we have also tested the solution procedure with different n values ($n = 2, 3$, in particular) for a few solutions, and the converged solutions were found to not depend on n at least in those cases (see also figure 6). However, if $n > 1$ is chosen, then it may be possible for the given solution procedure to capture incidentally unwanted exact solutions with nonlinearly saturated subharmonic/modulational instabilities. In such a case, the computed solutions would not be a homotopy of the original solution, as their primary time periodicity is no longer T. Furthermore, for a very large n, the Newton iteration does not converge quickly with a very small r due to the unstable nature of the solutions, and the related computation also becomes very expensive due to many simulations required over a long time interval. For this reason, $n = 1$ is chosen in the present study. In the absence of the spanwise wall oscillation, all the considered equilibria (EQ0, EQ1, EQ4 and EQ7) in this study satisfy the shift–reflect symmetry

$$[u, v, w, p](x, y, z) = [u, v, -w, p](x - L_x/2, y, -z), \tag{2.4}$$

where p is the pressure. However, under this symmetry, the streamwise uniform spanwise wall velocity vanishes, and the spanwise wall oscillation cannot be implemented.

https://doi.org/10.1017/jfm.2022.606 Published online by Cambridge University Press

Therefore, the condition (2.4) is relaxed for the computation of ECS in the presence of spanwise wall oscillation. The solutions are then computed using a pseudo arc-length continuation algorithm in the parameter space, (Re, A_w, T). The linear stability of each equilibrium solution is also performed by solving the corresponding eigenvalue problem via the Arnoldi iteration.

The edge state is also calculated using the standard bisection technique (Itano & Toh 2001; Skufca *et al.* 2006). This approach builds an initial guess by weighting two states, one of which is towards a turbulent state and the other towards a laminar state. For this calculation, we introduce the turbulent fluctuation energy averaged over a given computational domain,

$$(E_{uu}, E_{vv}, E_{ww}) = \frac{1}{2V}\int_{\Omega} (u'^2, v'^2, w'^2)/{U_w}^2 \,\mathrm{d}V, \tag{2.5}$$

where u', v' and w' are defined from the Reynolds decomposition $\boldsymbol{u} = \boldsymbol{U} + \boldsymbol{u}'$, with $\boldsymbol{U} = (U, V, W)$ being the streamwise, wall-normal and spanwise velocities averaged over time and in the wall-parallel directions, and $\boldsymbol{u}' = (u', v', w')$ the remaining velocity fluctuations. The bisection method is carried out by monitoring the cross-streamwise velocity fluctuation energy $(E_{vv} + E_{ww})$. The edge state investigated in this study is a periodic orbit obtained in the domain Ω_{HKW}, which is identical to the gentle periodic solution found by Kawahara & Kida (2001) and is denoted as PO in table 1. This periodic orbit is used as the initial guess in the Newton–Krylov–Hookstep solver with its specific period to complete its bifurcation diagram.

2.3. *Physical relevance to exact coherent states in fully developed turbulence*

Before presenting the result of the present study, some physical relevance of the ECS is discussed here. ECS refer to equilibrium solutions and unstable periodic orbits of the Navier–Stokes equations that resemble coherent structures and their dynamics. Typically, these solutions are unstable, and the turbulence trajectory visits them only transiently, making them difficult to be observed directly for a long time in typical laboratory experiments and numerical simulations (e.g. Hof *et al.* 2004; Kerswell & Tutty 2007). However, once many solutions are available, turbulence may be described as a random walk around these solutions. From this viewpoint, these solutions have been believed to form the state space skeleton of turbulence (Kerswell 2005; Eckhardt *et al.* 2007; Kawahara *et al.* 2012; Graham & Floryan 2021), playing a role of guiding the solution trajectory in the state space, and indeed this has been confirmed, at least in the minimal flow units considered in the present study (e.g. Gibson *et al.* 2009; Willis *et al.* 2013). Exact coherent states have also been computed for external flows where aerodynamic applications would be relevant (Khapko *et al.* 2013; Kreilos *et al.* 2016*a*,). Extending this approach to high Reynolds numbers is an important ongoing open research topic, although some previous efforts were made by modelling small scales using eddy viscosity (e.g. Hwang *et al.* 2016; Yang & Hwang 2019).

3. Results and discussion

3.1. *Bifurcation diagram of EQ states*

The bifurcation diagram of the various equilibrium solutions is shown in figure 1. Each of the solutions emerges through a saddle–node bifurcation. The solution that appears at the smallest Reynolds number is EQ0 from Nagata (1990) at critical Reynolds number

https://doi.org/10.1017/jfm.2022.606 Published online by Cambridge University Press

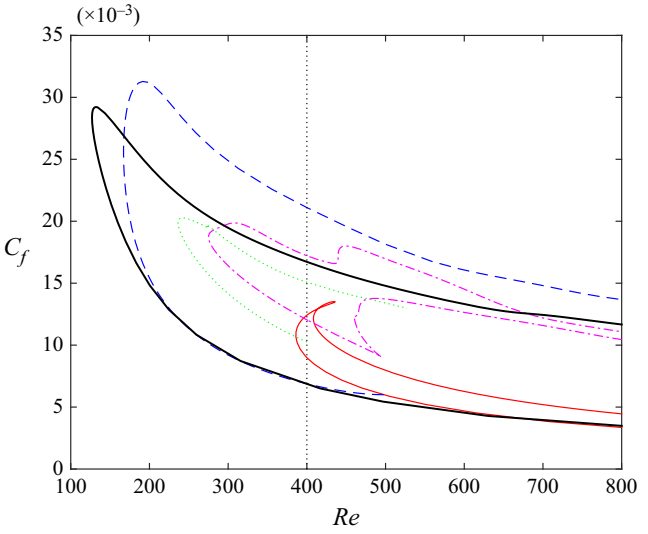


Figure 1. Bifurcation diagram of the equilibrium solutions in the C_f–Re plane: EQ0, black thick solid line; EQ1, red thin solid line; EQ4, pink dash-dotted line; EQ7, blue dashed line; PO, green dotted line. The vertical dashed line indicates $Re = 400$.

$Re_c \approx 127$, followed by EQ7 at $Re_c \approx 167$ from Gibson *et al.* (2009). The numerical continuation over the computational domain size indicates that EQ7 does not exist in the domain Ω_N, and EQ0 does not exist in the domain Ω_{HKW}. A large number of solutions, including EQ1, EQ4 and EQ7, were found previously in Ω_{HKW}. The bifurcation curves for EQ1 and EQ4 are more complicated. EQ1 appears through a saddle–node bifurcation at $Re_c = 386$, then second and third bifurcations occur on the upper branch at $Re_c = 408$ and 435, respectively. EQ4 first arises from a saddle–node bifurcation at $Re_c = 275$, then a second saddle–node bifurcation appears at $Re_c = 494$ from the lower branch, and at $Re_c = 438$ from the upper branch, respectively, giving rise to a new branch. For further details about the invariant solutions in Ω_{HKW}, the reader may refer to Gibson *et al.* (2009). The bifurcation curve for a periodic orbit (PO) identified in Ω_{HKW} is also presented in the figure by a green dotted line. The saddle–node bifurcation behaviour of PO is very similar to that of EQ0 and EQ7, with a critical Reynolds number located at $Re_c = 236.5$.

It is known that there is an optimal oscillation period at $T^+ \approx 100$ for spanwise wall oscillation control. Focusing on EQ0, we show that such an optimal oscillation period appears in the bifurcation diagram. Figure 2(*a*) presents the bifurcation curves for EQ0 with six different oscillation periods in the range $TU_w/h \in [1, 150]$ for a given wall oscillation amplitude $A_w/U_w = 0.1$. As the focus is on the saddle–node point, here the viscous wall units of the uncontrolled saddle–node point are used for the scaling of the oscillation period, which is more meaningful to identify the inner scaled optimal wall oscillation period. This gives $T^+ = 53$, 70.6, 106, 158.9, 211.9 and 264.9 for the six studied cases. Here, the amplitude A_w is selected deliberately to be small such that the solutions can exist at large oscillation periods, as will be discussed at the end of this section. As can be seen, the lower branch is much less affected by the control compared to the upper branch. The saddle–node point continues to move towards higher values as the oscillation period T^+ is increased, from $Re_c = 127.3$ of the uncontrolled case to $Re_c = 140.4$ at $T^+ = 106$ and $Re_c = 142.5$ at $T^+ = 211.9$, then moves back to $Re_c = 142.2$ at $T^+ = 264.9$. This indicates that the emergence of the unstable solutions

https://doi.org/10.1017/jfm.2022.606 Published online by Cambridge University Press

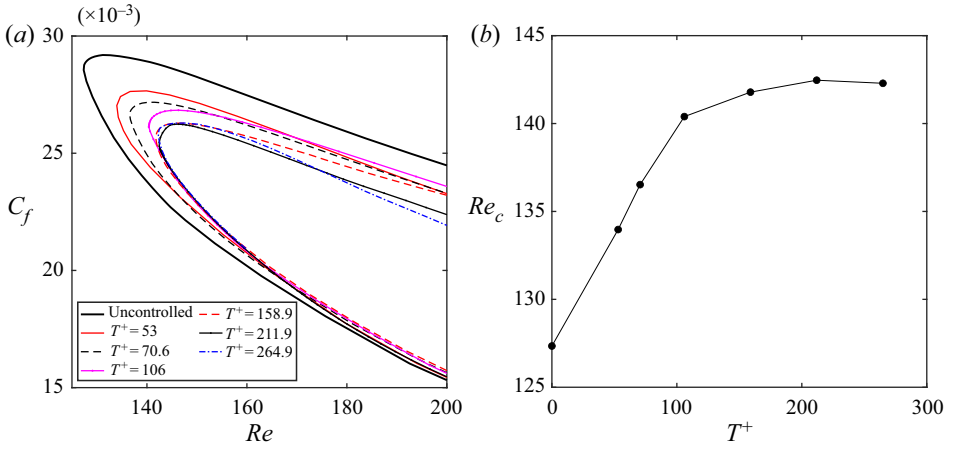


Figure 2. (*a*) Plots of C_f–Re bifurcation curves for EQ0 with different oscillation periods at $A_w/U_w = 0.1$. (*b*) The saddle–node Reynolds number variation with the oscillation period. Here, the wall units of the uncontrolled case at the saddle–node point are used for the scaling of the wall oscillation periods.

is delayed to higher Reynolds numbers, implying the suppression of these solutions, a primitive form of turbulence. We note that the decreasing rate of Re_c becomes slower eventually as T^+ becomes larger, and Re_c increases only slightly for $T^+ > 106$. The skin friction of the upper branch does not decrease after $T^+ > 70.6$ at $Re \approx 170$. For larger oscillation periods, it was difficult to obtain converged solutions, and we were not able to continue numerically for $T^+ > 264.9$ with EQ0. The critical Reynolds number variation at the saddle–node point with the wall oscillation period is presented in figure 2(*b*). It is clear that the saddle–node Reynolds number saturates for $T^+ > 106$, consistent with the optimal oscillation period (i.e. $T^+ \approx 100$) as observed in the DNS data as well as our previous bifurcation study of the wall-attached ECS under spanwise wall oscillation in Poiseuille flow (Yang & Hwang 2019), although the present solution shows a broader optimal T^+ regime for drag reduction compared to that of fully developed turbulence at much higher Reynolds numbers.

In figure 3, we show the bifurcation curves of the equilibrium solutions EQ0, EQ1, EQ4 and EQ7 in the C_f–Re plane for different spanwise wall oscillation amplitudes, each of which has a lower and an upper branch subject to the spanwise wall oscillation. The thick solid lines represent the uncontrolled reference cases of each equilibrium solution. For each solution, we fix the wall oscillation period T^+ and choose different values of amplitude A_w^+. As mentioned in table 2, here the viscous inner units of the corresponding uncontrolled DNS of each computational domain at $Re = 400$ are used for the scaling. The upper branch of each equilibrium solution pair shows a significant skin-friction reduction as A_w^+ is increased. This strong effect on the upper branch of each solution leads to the emergence of sophisticated bifurcations along the upper branch on increasing A_w^+ (figures 3(*a*,*b*), in particular), although there is no common trend in those bifurcations. It is noted that the monotonic decrease of the C_f value of the upper branch solution with the increase of A_w^+ is analogous to the effect of A_w^+ on turbulent drag reduction in fully developed turbulence at much higher Reynolds numbers (Quadrio & Ricco 2004; Quadrio *et al.* 2009). On the contrary, the effect on the lower branch is nearly negligible over almost the entire range of Reynolds numbers. The effect of control on the lower branch is, however, not monotonic. We observe a slight decrease of C_f for sufficiently high Reynolds

https://doi.org/10.1017/jfm.2022.606 Published online by Cambridge University Press

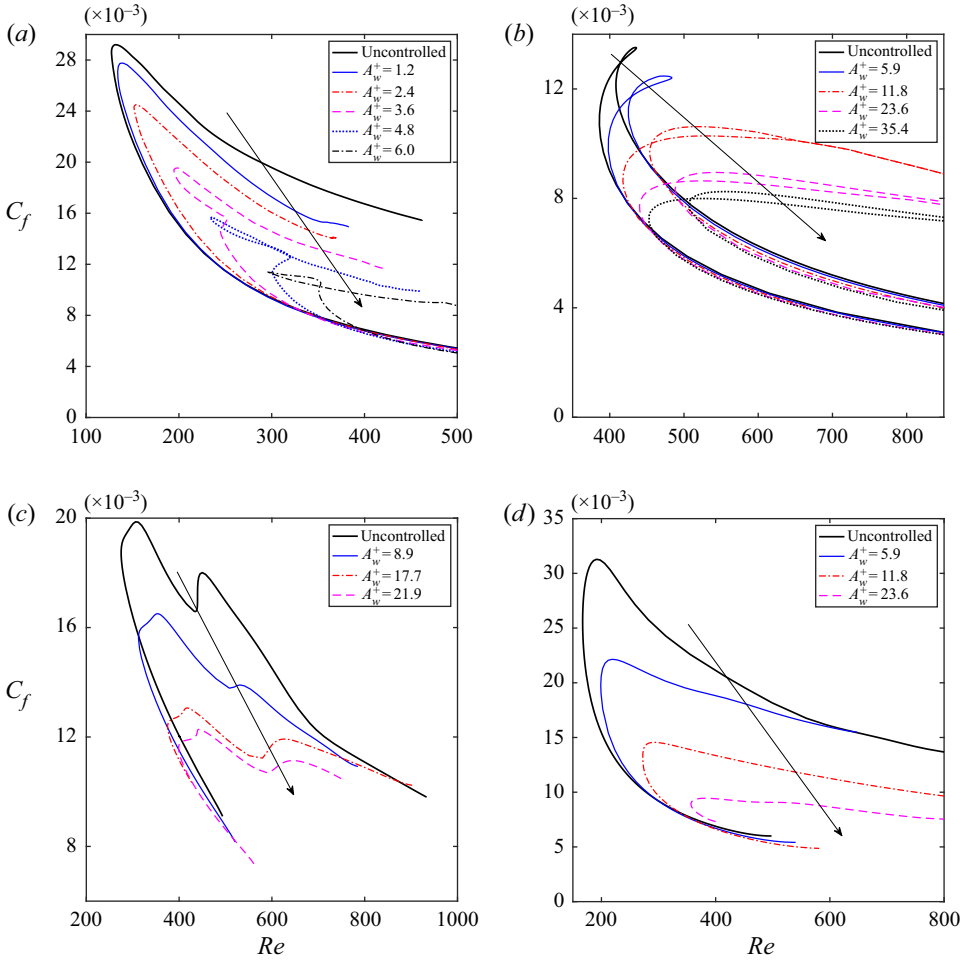


Figure 3. Bifurcation curves at different values of wall oscillation amplitudes A_w^+ in the C_f–Re plane: (*a*) EQ0 with $T^+ = 79.8$; (*b*) EQ1 with $T^+ = 14.3$; (*c*) EQ4 with $T^+ = 14.3$; (*d*) EQ7 with $T^+ = 28.7$. Thick solid curves correspond to the uncontrolled reference cases. The arrows indicate increasing A_w^+.

numbers, while the skin-friction coefficient near the saddle–node point increases until the lower and upper branches collapse and disappear. As a consequence, the saddle–node bifurcation points move towards higher Reynolds numbers, indicating stabilisation of the equilibrium solutions.

Figure 4 shows further the bifurcation curves of the skin-friction coefficient with respect to the wall oscillation amplitude A_w^+ for various oscillation periods T^+ at $Re = 400$. In general, commonly the upper branches of the solutions exhibit a significant reduction in C_f on increasing A_w^+, consistent with figure 3. On the contrary, C_f values of the lower branches depend on the individual solutions and the time period considered (see figure 4). However, the significant reduction of C_f in the upper branch leads the two branches to meet at a certain value of A_w^+, forming a saddle–node bifurcation in terms of A_w^+. An increase of the wall oscillation period T^+ yields the solutions to form the saddle–node point at lower values of A_w^+. However, it should be mentioned that this behaviour may well be true only

https://doi.org/10.1017/jfm.2022.606 Published online by Cambridge University Press

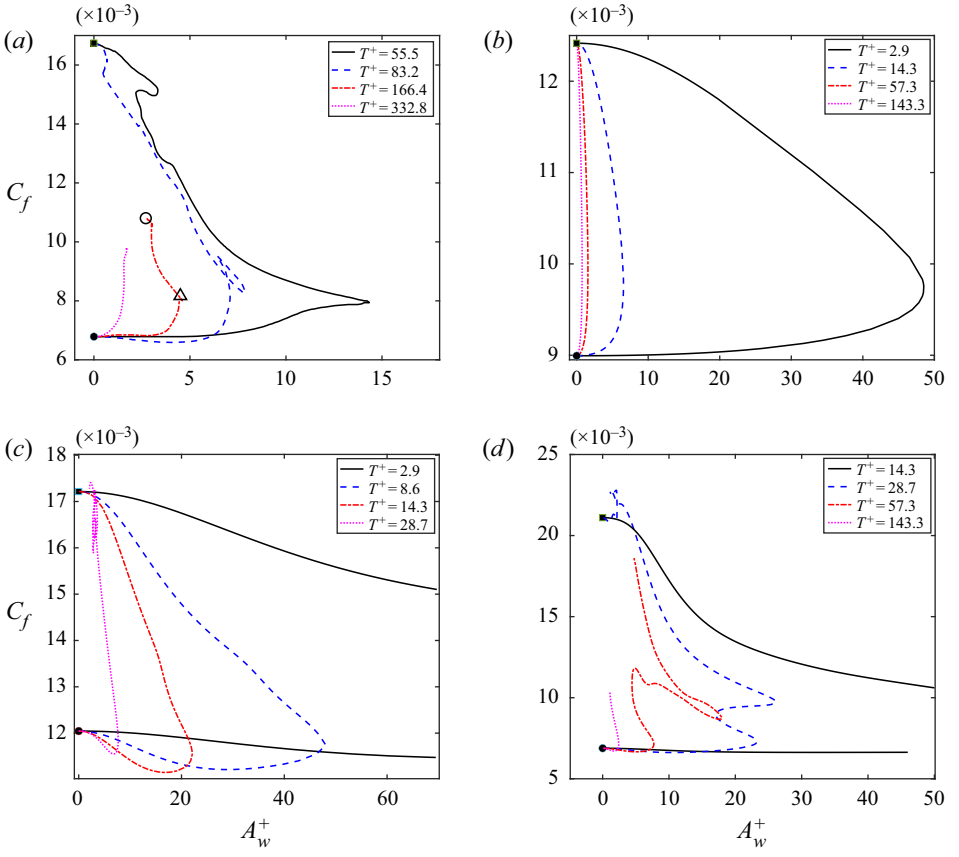


Figure 4. Bifurcation curves C_f–A_w^+ for different oscillation periods T^+ at $Re = 400$: (*a*) EQ0, (*b*) EQ1, (*c*) EQ4, (*d*) EQ7. The black filled circles and squares indicate the lower and upper branch solutions, respectively, at $A_w^+ = 0$. The open circle and triangle in (*a*) indicate, respectively, case A ($Re = 400$, $T^+ = 166.4$, $A_w^+ = 2.6$) and case B ($Re = 400$, $T^+ = 166.4$, $A_w^+ = 4.4$) presented in table 2.

for the values of T^+ considered here, as the numerical continuation of the solutions (upper branches, in particular) is found to be difficult for very large T^+.

3.2. *Statistics*

The spanwise wall oscillation generates an unsteady near-wall spanwise shear layer referred to as the Stokes layer (according to the Stokes' second problem). For the laminar case, the flow introduced by the spanwise wall motion is decoupled from the streamwise flow, and the unsteady Stokes layer can be expressed analytically as (Schlichting 1979)

$$W(y, t) = A_w \, \mathrm{e}^{-\eta} \sin(2\pi t/T - \eta), \tag{3.1}$$

where $\eta = -y\sqrt{\pi \, Re/T}$ is related to the Stokes layer thickness. A larger spanwise wall oscillation period leads to a thicker Stokes layer, and for a given oscillation period, the wall oscillation amplitude only affects the spanwise displacement of the wall. Because of the presence of two walls, (3.1) is, however, not valid in this context, especially when the Stokes layer thickness is comparable to the half channel width. Therefore, we have considered further the analytical solution for the uniform spanwise wall oscillation

https://doi.org/10.1017/jfm.2022.606 Published online by Cambridge University Press

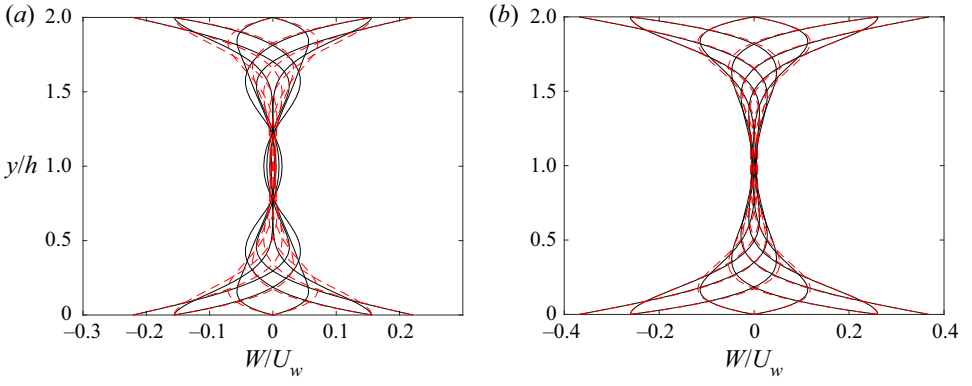


Figure 5. Unsteady spanwise Stokes layer at 8 equally separated phases for: (*a*) case A ($Re = 400$, $T^+ = 166.4$, $A_w^+ = 2.6$), and (*b*) case B ($Re = 400$, $T^+ = 166.4$, $A_w^+ = 4.4$). The solid and dashed lines indicate, respectively, the equilibrium state of EQ0 and the analytical solution in (3.2).

problem in channel flow, derived by Jozsa (2019). This solution is given by

$$W(y,t) = \mathrm{Re}\left(A_w \exp(\mathrm{i}2\pi t/T)\,\frac{\cos(y\sqrt{-\mathrm{i}2\pi\, Re/T})}{\cos(\sqrt{-\mathrm{i}2\pi\, Re/T})}\right), \tag{3.2}$$

where Re(·) indicates the real part.

In figure 5, we present the Stokes layer at eight equally separated phases for cases A and B of the EQ0 state (see also figure 4*a*). With the given wall oscillation period $T^+ = 166.4$, the analytical profiles of the Stokes layer decay to zero only near the channel centre. As the spanwise Stokes layer is affected by the equilibrium state, the Stokes layer profiles of EQ0 under control start to deviate from the analytical ones. We note that such a deviation is small in the region close to the wall, but becomes large away from the wall (see figure 5*a*). In general, it is found that at a small oscillation period, the Stokes layer is thin and the agreement with the analytical solution is improved (not shown here). This is because the Stokes layer of the equilibrium state is obtained from the spanwise mean momentum balance and is determined by the contribution from the wall-normal gradient of the spanwise Reynolds shear stress term $\partial\overline{v'w'}/\partial y$, which has been found to increase with the oscillation period and the Reynolds number (Ricco & Quadrio 2008; Yang 2016). At a higher drag state, such as case A shown in figure 5(*a*), the Stokes layer of the equilibrium state differs largely from that of the analytical solution in (3.2), and some oscillating flow even appears in the channel centre. On the contrary, the agreement of the Stokes layer between the equilibrium state and the analytical solution is greatly improved for a lower drag state of case B (figure 5*b*). It is noted that under the control parameters for cases A and B, the difference between the analytical solutions from (3.1) and (3.2) is small.

The time variations of the instantaneous skin-friction coefficient $C_{f,t}$ for cases A and B are shown in figure 6. For the spanwise wall oscillation cases, the statistics is sampled and averaged over one single wall oscillation period for the converged solution, i.e. $C_f = (1/T)\int_0^T C_{f,t}\,\mathrm{d}t$. Each solution is computed and compared with two different values of n (i.e. $n = 1, 2$) used for the calculation (see § 2.2). As expected, the converged solution does not depend on n, except that the solution with $n = 2$ simply repeats that of $n = 1$ twice. As already mentioned for figure 4(*a*), case A is a higher drag state with $C_f = 0.0107$, while case B is a lower drag state with $C_f = 0.0079$. Based on the

https://doi.org/10.1017/jfm.2022.606 Published online by Cambridge University Press

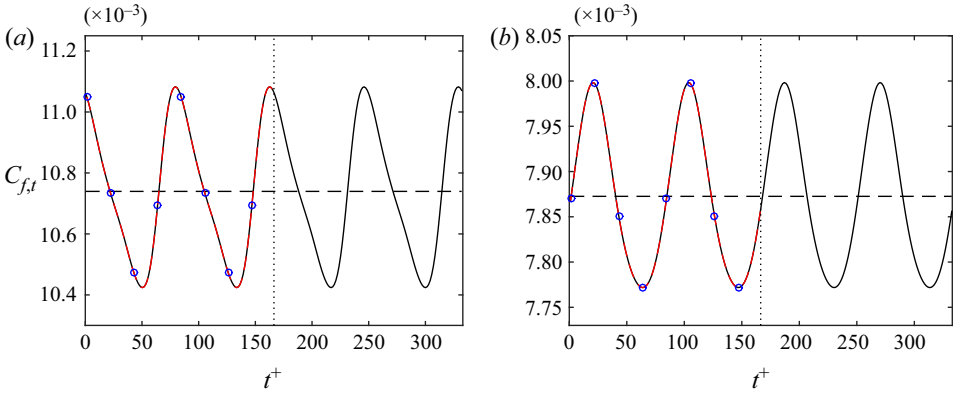


Figure 6. Variation of instantaneous skin-friction coefficient $C_{f,t}$ over time for (*a*) case A ($Re = 400$, $T^+ = 166.4$, $A_w^+ = 2.6$), and (*b*) case B ($Re = 400$, $T^+ = 166.4$, $A_w^+ = 4.4$). The red dashed (black solid) lines are for equilibrium solutions computed with $n = 1$ ($n = 2$) in the Newton solver. The horizontal lines indicate the mean value of the skin-friction coefficient, i.e. $C_f = 0.0107$ and 0.0079 for cases A and B, respectively. The vertical dotted lines mark one wall oscillation period, $T^+ = 166.4$. The blue circles mark the 8 equally separated phases investigated for each case, i.e. $\phi = 0, \pi/4, \pi/2, 3\pi/4, \pi, 5\pi/4, 3\pi/2, 7\pi/4$.

derivation of the wave pattern of $C_{f,t}$ in time compared to the sinusoidal wall oscillation wave, the equilibrium solution of case A is modulated more strongly by the spanwise wall oscillation compared to that of case B, and each solution has the $C_{f,t}$ variation of 3.2 % and 1.6 % during one wall oscillation period, respectively. It is noted that the skin-friction coefficient for the upper branch of the uncontrolled EQ0 state at $Re = 400$ is $C_f = 0.0167$, thus the two controlled cases have drag reduction $\mathcal{DR} = 35.9\,\%$ and 52.7 %, respectively.

Figure 7 shows the root-mean-square (r.m.s.) velocity components, i.e. u^+_{rms}, v^+_{rms}, w^+_{rms}, and the streamwise Reynolds shear stress $-\overline{u'v'}^+$ profiles for case A at 8 equally separated phases (dotted lines) over one wall oscillation period (see symbols in figure 6*a*). The phase variation in the statistics becomes clear with a modest value, which corresponds to 3.2 % variation in the skin friction (figure 6*a*). It is interesting to note that the r.m.s. profiles of the controlled state A appear to sit between those of the upper- and lower-branch solutions. For example, the upper-branch solution shows a strong near-wall peak in u^+_{rms}, while such a peak is located in the channel centre for the lower-branch solution. The controlled state A exhibits the two features in a mixed manner – the strength of u^+_{rms} in the channel centre is increased compared to the upper branch, while the u^+_{rms} peak in the near-wall region is weakened (figure 7*a*). The rest of the profiles behave in a similar manner (figures 7*b–d*). Furthermore, the reduction of $-\overline{u'v'}^+$ over the entire wall-normal locations compared to the upper-branch solution indicates a drag reduction according to the FIK identity (Fukagata, Iwamoto & Kasagi 2002) – indeed, 35.9 % of $\mathcal{DR}$ from the upper-branch solution is observed. Similar statistics features are also observed from the other exact coherent states in the domain Ω_{HKW}, which are presented in Appendix B.

3.3. *Streak variation*

Now, the time and space variations of the streaks are studied using cases A and B of EQ0. We note that the choice of EQ0 is made because it appears to be more useful than the

https://doi.org/10.1017/jfm.2022.606 Published online by Cambridge University Press

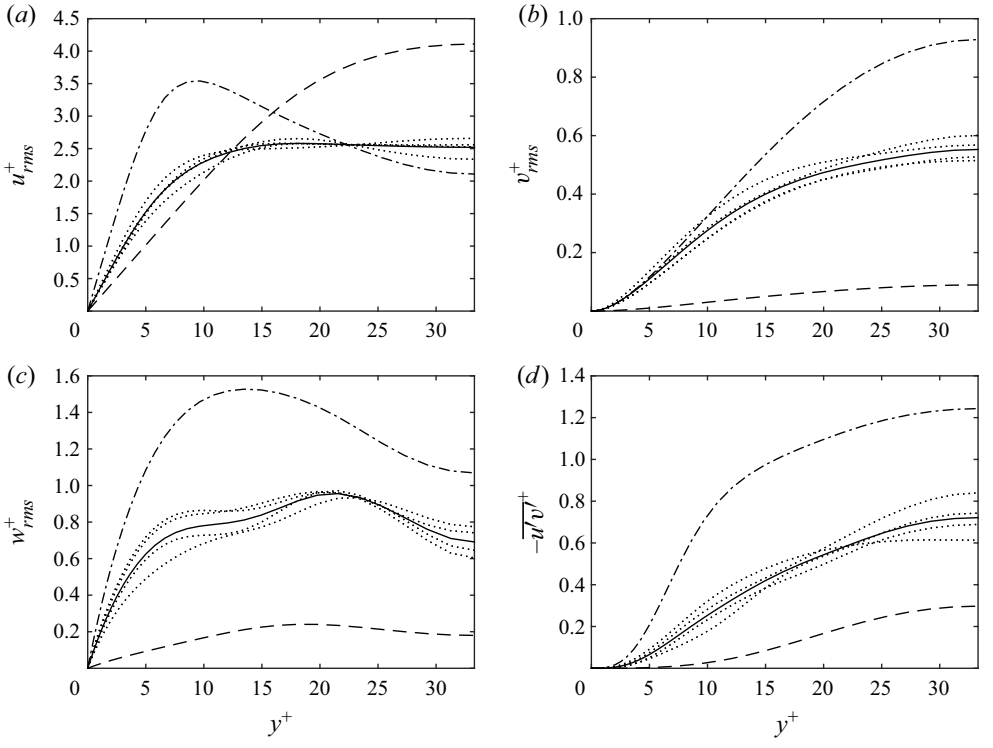


Figure 7. Root-mean-square (r.m.s.) velocity profiles scaled with viscous inner units of the uncontrolled DNS for case A ($Re = 400$, $T^+ = 166.4$, $A_w^+ = 2.6$): (*a*) u^+_{rms}, (*b*) v^+_{rms}, (*c*) w^+_{rms}, and (*d*) $-\overline{u'v'}^+$. Dash-dotted (dashed) lines represent the upper (lower) branch of the uncontrolled state, and dotted lines indicate the controlled state at 8 equally separated phases, with the mean profile indicated by the solid line.

other solutions for the following reasons. First, currently EQ0 is known as the invariant solution emerging at the lowest Reynolds number in plane Couette flow. Importantly, turbulence emerges directly from the upper branch of EQ0 through a bifurcation cascade (Kreilos & Eckhardt 2012) – note that all the other equilibrium solutions considered here do not have this feature. Furthermore, the skin friction of the upper branch of EQ0, often believed to be more relevant to the turbulent state, is $C_f = 0.0168$ at $Re = 400$, not very far from the time-averaged turbulent state with $C_f = 0.0138$ at the same Reynolds number. Finally, at $Re = 400$, the lower branch of EQ0 is the edge state in the domain Ω_N (Schneider *et al.* 2008). A particular feature for spanwise wall oscillation control of turbulence is the modulation of the near-wall streaks by the Stokes layer, which has been studied extensively using instantaneous flow fields or conditionally averaged flow structures obtained from DNS. As a result, some key dynamical features of the controlled flow may not be well observed in the complex three-dimensional flow field or are averaged out in the conditional flow fields. Such a drawback may be bypassed by inspecting some equilibrium solutions modulated by the Stokes layer, as they are the exact solutions of the Navier–Stokes equations.

Figure 8 presents the streamwise-averaged streaks visualised by $\langle u' \rangle_x$ contour and the vortical motions visualised by $(\langle v' \rangle_x, \langle w' \rangle_x - \langle w' \rangle_{x,z})$ vectors for cases A and B. The features of the upper- and lower-branch solutions of EQ0 at $Re = 400$ without control are shown in the top row of figure 8. It is clear that the shapes of the low- and high-speed

https://doi.org/10.1017/jfm.2022.606 Published online by Cambridge University Press

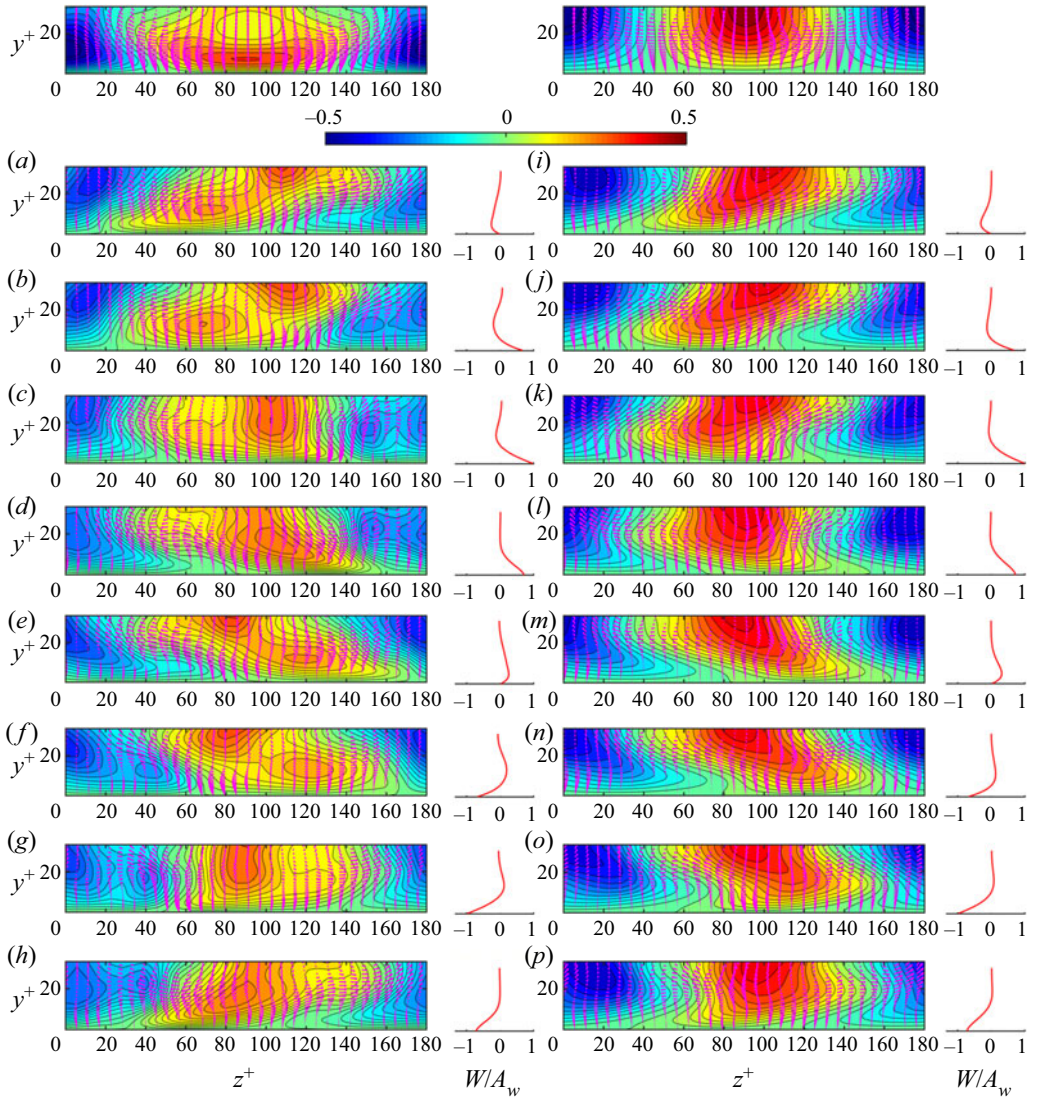


Figure 8. Streamwise-averaged low- and high-speed streaks (contour by $\langle u' \rangle_x$) and in-plan vortex (arrows plotted by $(\langle v' \rangle_x, \langle w' \rangle_x - \langle w' \rangle_{x,z})$) variation during one oscillation period for (*a–h*) case A ($Re = 400$, $T^+ = 166.4$, $A_w^+ = 2.6$), and (*i–p*) case B ($Re = 400$, $T^+ = 166.4$, $A_w^+ = 4.4$), at different phases: (*a,i*) $\phi = 0$; (*b,j*) $\phi = \pi/4$; (*c,k*) $\phi = \pi/2$; (*d,l*) $\phi = 3\pi/4$; (*e,m*) $\phi = \pi$; (*f,n*) $\phi = 5\pi/4$; (*g,o*) $\phi = 3\pi/2$; (*h,p*) $\phi = 7\pi/4$. The Stokes profiles at the corresponding phases are shown on the right-hand side of each contour plot. The top row presents the flow fields of the corresponding upper- and lower-branch solutions of uncontrolled EQ0 at $Re = 400$. Viscous inner units of the uncontrolled DNS case are used for the scaling.

streaks of the lower-branch solution are almost symmetrical to each other, while this is not the case for the upper-branch solution, with the high-speed streak spreading a much wider area in the spanwise direction of the near-wall region and the low-speed streak more localised. Therefore, in the upper-branch solution, the high-speed streak is expected to make a strong contribution to the elevation of local skin friction, and

https://doi.org/10.1017/jfm.2022.606 Published online by Cambridge University Press

this should be significantly greater than the local reduction created by the low-speed streak.

Once spanwise wall oscillation is applied, the streaks are modulated significantly by the Stokes layer. For case A, (figures 8*a–h*), similarly to the upper-branch solution of the uncontrolled case, the high-speed streak is stronger than the low-speed one. However, under the control, the high-speed streak in the near-wall region is tilted strongly in the spanwise direction. In particular, the near-wall part of the high-speed streak penetrates deeply underneath the low-speed streak, and vice versa. Such a spanwise motion appears to enhance fluid mixing between the low- and high-speed streaks. Therefore, the locally high-friction region from the high-speed streaks is balanced out with the locally low-friction region from the low-speed streaks, resulting in a drag reduction – indeed, the asymmetry between the low- and high-speed streaks appears to be weaker than that of the upper-branch solution of the uncontrolled case (see figures 8*d*,*h*). For case B (figures 8*i–p*), a lower drag state, the low- and high-speed streaks are almost symmetric to each other, and their movements in the spanwise direction are nearly in phase. Moreover, the low- and high-speed streaks have the largest fluctuation in the channel centre. We also note that the streak variation in the spanwise direction is very similar to the conditionally averaged results in the DNS study by Touber & Leschziner (2012). This indicates that the equilibrium solutions in this study do capture some important dynamics of the near-wall flow under the spanwise wall oscillation, although the Reynolds number considered here is much lower than that of Touber & Leschziner (2012).

To explore further the streak angle variation during one wall oscillation period, the high-speed streak and vortical structure are visualised in figures 9 and 10 for cases A and B, respectively. At first glance, the structures for case A are more active than those for case B. During one oscillation period, two dominant streak-tilting angles are seen with opposite sign, as also observed in previous DNS studies (Touber & Leschziner 2012; Chung *et al.* 2013). Each of these angles is seen dominantly for half an oscillation period. For cases A and B, these tilting angles of the streaks are found to be $\alpha \approx \pm 18^\circ$ and $\alpha \approx \pm 14^\circ$, respectively. By monitoring the evolution of the streaks in figure 9, the high-speed streak is first tilted in the negative spanwise direction until $\phi = \pi/2$, then breaks down suddenly into two streaks, a stronger one that grows fast, and a weaker one that dissipates quickly. By checking the temporal skin-friction variation of case A (see figure 6*a*), it is found that $C_{f,t}$ reaches its minimum value at the streak breakdown stage, while it reaches the peak value at the phase with the strongest streak. For case B (figure 6*b*), the switch from a negatively tilted streak to a positively tilted one ($\phi = \pi/2$–$3\pi/4$) is also very quick, but the streak breakdown process is not observed clearly as in case A.

Finally, it is worth mentioning that the tilting dynamics of the near-wall streaks is found to depend strongly on the strength of the Stokes layer. Unfortunately, this feature does not allow for a direct comparison with that observed in the previous DNS at high Reynolds numbers (Touber & Leschziner 2012). In fact, as can be seen from figure 4, the equilibrium solutions of EQ1, EQ4 and EQ7 under the spanwise wall oscillation disappear at large wall oscillation amplitudes and periods. In other words, the Stokes layer, which was able to be examined here, was not strong enough to generate a large variation in the streak angle.

3.4. *State space dynamics*

Now, to visualise the relevant state space using state portraits, suitable observables are defined. Similarly to previous studies (e.g. Kawahara & Kida 2001; Ibrahim *et al.* 2019),

https://doi.org/10.1017/jfm.2022.606 Published online by Cambridge University Press

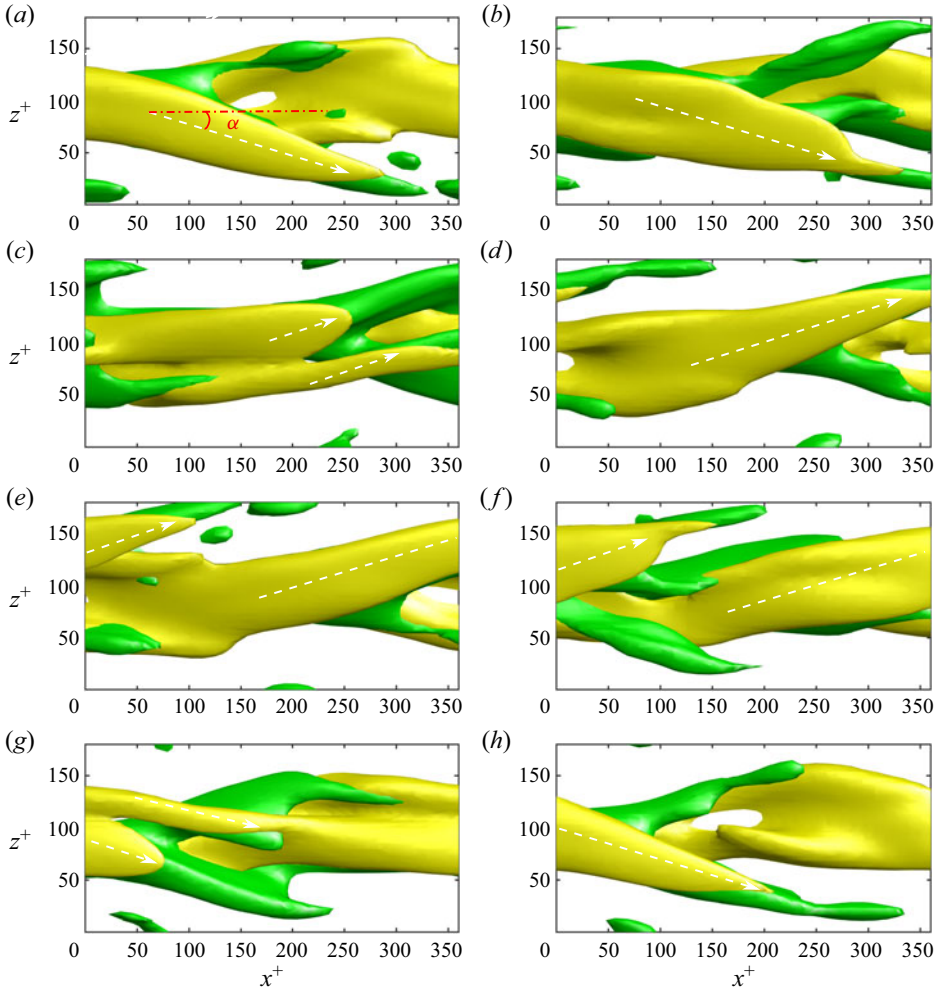


Figure 9. Streak variation viewed from the bottom of the channel during one oscillation period for case A ($Re = 400$, $T^+ = 166.4$, $A_w^+ = 2.6$) at different phases: (*a*) $\phi = 0$, (*b*) $\phi = \pi/4$, (*c*) $\phi = \pi/2$, (*d*) $\phi = 3\pi/4$, (*e*) $\phi = \pi$, (*f*) $\phi = 5\pi/4$, (*g*) $\phi = 3\pi/2$, and (*h*) $\phi = 7\pi/4$. A yellow isosurface ($u'^+ = 2.0$) indicates the high-speed streak, and a green isosurface ($v'^+ = -0.2$) represents the vortical structure. The arrows represent the streak angle. Viscous inner units of the uncontrolled DNS are used for the scaling.

the volume-averaged equation for the mean kinetic energy (MKE) is first introduced:

$$\frac{\mathrm{d}E_U}{\mathrm{d}t} = \underbrace{\frac{U_w \tau_{uw}}{h}}_{\mathcal{I}_U} \underbrace{- \frac{1}{V}\int_\Omega -\langle u'v'\rangle_{x,z}\frac{\partial U}{\partial y}\,\mathrm{d}V}_{\mathcal{P}_{uv}} \underbrace{- \frac{\nu}{V}\int_\Omega \left(\frac{\partial U}{\partial y}\right)^2 \mathrm{d}V}_{\mathcal{D}_U}$$
$$+ \underbrace{\frac{W_w \tau_{ww}}{h}}_{\mathcal{I}_W} \underbrace{- \frac{1}{V}\int_\Omega -\langle v'w'\rangle_{x,z}\frac{\partial W}{\partial y}\,\mathrm{d}V}_{\mathcal{P}_{vw}} \underbrace{- \frac{\nu}{V}\int_\Omega \left(\frac{\partial W}{\partial y}\right)^2 \mathrm{d}V}_{\mathcal{D}_W}, \tag{3.3a}$$

https://doi.org/10.1017/jfm.2022.606 Published online by Cambridge University Press

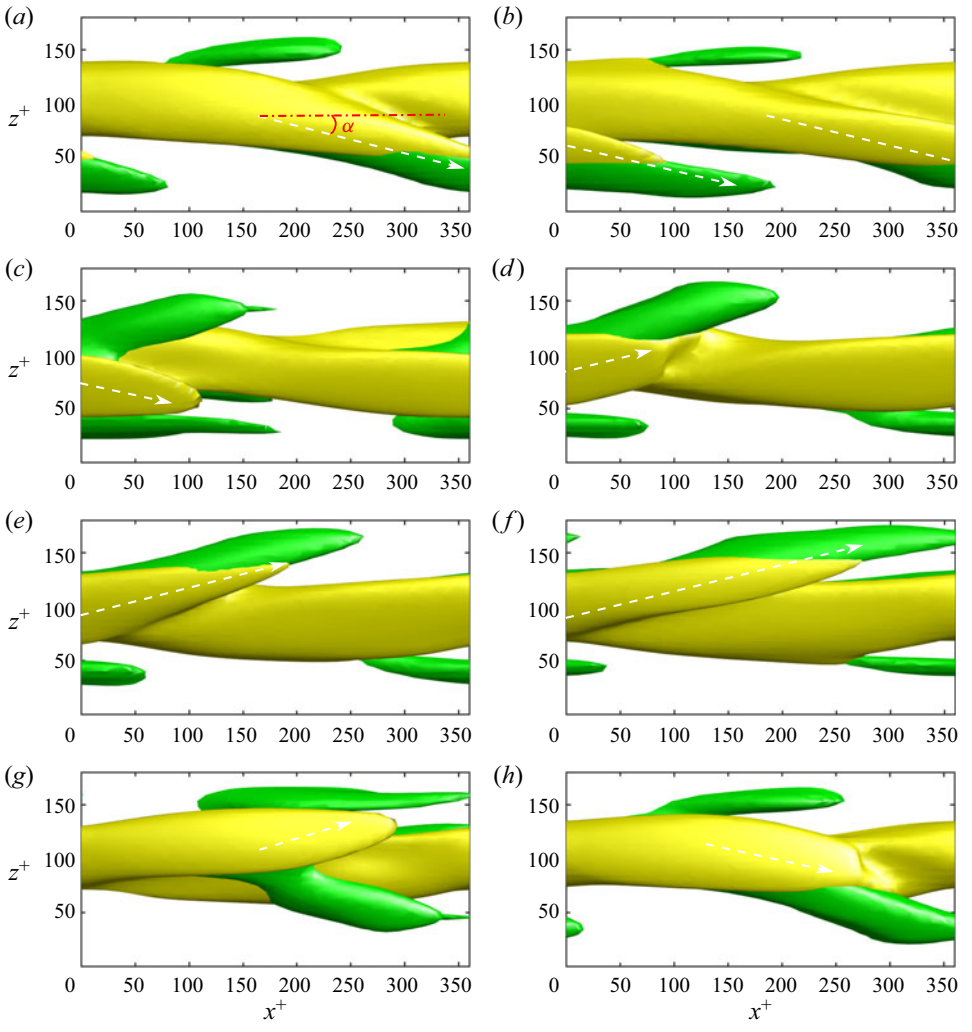


Figure 10. Streak variation viewed from the bottom of the channel during one oscillation period for case B ($Re = 400$, $T^+ = 166.4$, $A_w^+ = 4.4$) at different phases: (*a*) $\phi = 0$, (*b*) $\phi = \pi/4$, (*c*) $\phi = \pi/2$, (*d*) $\phi = 3\pi/4$, (*e*) $\phi = \pi$, (*f*) $\phi = 5\pi/4$, (*g*) $\phi = 3\pi/2$, and (*h*) $\phi = 7\pi/4$. A yellow isosurface ($u'^+ = 2.0$) indicates the high-speed streak, and a green isosurface ($v'^+ = -0.1$) represents the vortical structure. The arrows represent the streak angle. Viscous inner units of the uncontrolled DNS are used for the scaling.

with the MKE given by

$$E_U = \frac{1}{V}\int_{\Omega} \boldsymbol{U}\cdot\boldsymbol{U}\,\mathrm{d}V, \tag{3.3b}$$

where Ω ($= \Omega_N$ or Ω_{HKW}) is the given computational domain, U_w and W_w are the streamwise and spanwise velocities at the wall, and $\tau_{uw} = \mu\langle\partial u/\partial y|_{y=0,2h}\rangle_{x,z}$ and $\tau_{ww} = \mu\langle\partial w/\partial y|_{y=0,2h}\rangle_{x,z}$ are the spatial averaged streamwise and spanwise wall shear stresses, respectively. The terms indicated by $\mathcal{I}_U$, $\mathcal{P}_{uv}$ and $\mathcal{D}_U$ in the first line of (3.3*a*) are the rate of energy input, the rate of energy transport by streamwise mean shear to turbulent kinetic energy (TKE), and the dissipation rate by the streamwise mean velocity, respectively. Similarly, the three terms in the second line, i.e. $\mathcal{I}_W$, $\mathcal{P}_{vw}$ and $\mathcal{D}_W$, correspond to the

https://doi.org/10.1017/jfm.2022.606 Published online by Cambridge University Press

rate of energy input by the spanwise wall oscillation, the rate of energy transport by the spanwise mean shear to TKE, and the dissipation rate by the spanwise mean velocity.

The volume-averaged equation for TKE is also written as

$$\frac{\mathrm{d}E_{\boldsymbol{u}}}{\mathrm{d}t} = \underbrace{\frac{1}{V}\int_{\Omega} -\langle u'v'\rangle_{x,z}\frac{\partial U}{\partial y}\,\mathrm{d}V}_{\mathcal{P}_{uv}} + \underbrace{\frac{1}{V}\int_{\Omega} -\langle v'w'\rangle_{x,z}\frac{\partial W}{\partial y}\,\mathrm{d}V}_{\mathcal{P}_{vw}} - \underbrace{\frac{\nu}{V}\int_{\Omega}\langle(\boldsymbol{\nabla}\boldsymbol{u}')^2\rangle_{x,z}\,\mathrm{d}V}_{\mathcal{D}_{\boldsymbol{u}}}, \tag{3.4}$$

with $E_{\boldsymbol{u}} = E_{uu} + E_{vv} + E_{ww}$ from (2.5). Here, the first two terms, $\mathcal{P}_{uv}$ and $\mathcal{P}_{vw}$, are identical to those of (3.3*a*), but with opposite signs, emerging as the rate of turbulence production by streamwise and spanwise mean shear, and the last term, $\mathcal{D}_{\boldsymbol{u}}$, is the TKE dissipation. For details about the derivation of (3.3*a*) and (3.4), the reader may refer to Ricco *et al.* (2012). Finally, the rate of total energy input and dissipation are given by $\mathcal{I} \equiv \mathcal{I}_U + \mathcal{I}_W$ and $\mathcal{D} \equiv \mathcal{D}_U + \mathcal{D}_W + \mathcal{D}_{\boldsymbol{u}}$, respectively.

Two state portraits from the domain Ω_{HKW} at $Re = 400$ are plotted in the $\mathcal{I}_U$–$\mathcal{D}_{\boldsymbol{u}}$ and E_{uu}–E_{vv} planes, respectively, and they are shown in figure 11. Here, the equilibrium solutions and periodic edge state in the presence of control are presented by averaging over a single wall oscillation period, while the turbulent state is shown with its time trajectory. When the control is applied with $A_w^+ = 17.7$ and $T^+ = 14.3$, the non-zero spanwise energy input $\mathcal{I}_W$ is given for all the solutions (closed symbols). Figure 11(*a*) shows that the control pushes all the solutions towards the laminar state in the direction of decreasing $\mathcal{I}_U$ and $\mathcal{D}_{\boldsymbol{u}}$. Indeed, at these specific parameters, all the solutions indicate a reduction of the drag because $\mathcal{I}_U$ in (3.3*a*) is proportional to the streamwise wall shear stress (figure 4). We observe that the upper branches and the mean turbulent state are much more affected by the control than the lower branches. Indeed, the lower branches $\mathrm{EQ4}_L$ and $\mathrm{EQ7}_L$ show 7.3 % and 3.2 % of $\mathcal{DR}$, respectively; the upper branches $\mathrm{EQ4}_U$ and $\mathrm{EQ7}_U$ show 25.8 % and 33.7 % of $\mathcal{DR}$, respectively, and the mean turbulent state shows 10.9 % of $\mathcal{DR}$. The state portrait of the streamwise kinetic energy fluctuation E_{uu} against the wall-normal kinetic energy fluctuation E_{vv} shown in figure 11(*b*) indicates similar results. The control is seen to be responsible for a reduction in the wall-normal velocity fluctuation, which results in a decrease in E_{vv} and pushes the solutions towards the laminar state. The state portraits indicate that the region of the state space where the turbulent state is organised is reduced by the spanwise wall oscillation. Furthermore, the state portraits also show that the state space distances between the upper and lower branches of each solution pair presented at least in figure 11 are reduced, indicating stabilisation of turbulence.

The stability of the exact coherent states is also examined. Since the exact coherent states in the present study are stationary in space and are periodic in time under the spanwise wall oscillation, the normal-mode ansatz for the Floquet analysis yields the following form for a small perturbation around them:

$$\boldsymbol{u}(x, y, z, t) = \boldsymbol{Q}(x, y, z, t)\,\hat{\boldsymbol{u}}(x, y, z)\,\mathrm{e}^{\lambda t} + c.c, \tag{3.5}$$

where λ is the complex Floquet exponent (eigenvalue), $\hat{\boldsymbol{u}}(x, y, z)$ is the corresponding complex Floquet eigenmode, $\boldsymbol{Q}(x, y, z, t) = \boldsymbol{Q}(x, y, z, t + T)$ and $\boldsymbol{Q}(x, y, z, 0) = \boldsymbol{I}$, with $\boldsymbol{I}$ being the identity operator. We note that (3.5) is extendable for the stability of the uncontrolled steady solutions with $\boldsymbol{Q}(x, y, z, t) = \boldsymbol{I}$. Figure 12 shows the eigenspectra of the lower and upper branches of EQ4 and EQ7, with the real and imaginary parts representing the growth rate and frequency of the eigenmodes, respectively. We observe that for the upper-branch solutions of both cases, where the control yields a drag reduction, the growth rates of the eigenmodes are also decreased, indicating stabilisation. On the

https://doi.org/10.1017/jfm.2022.606 Published online by Cambridge University Press

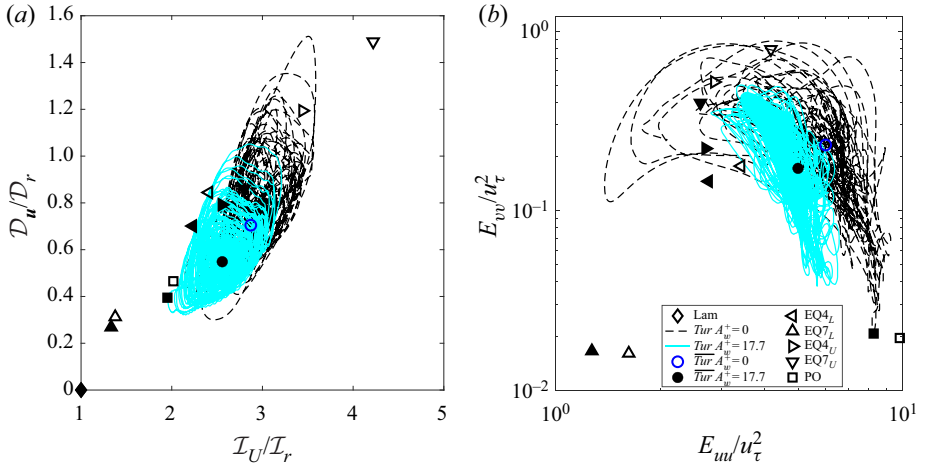


Figure 11. State portraits for controlled ($A_w^+ = 17.7$, $T^+ = 14.3$) and uncontrolled states at $Re = 400$ in (a) the $\mathcal{I}_U$–$\mathcal{D}_{\boldsymbol{u}}$ plane (with $\mathcal{I}_r$ and $\mathcal{D}_r$ the energy input and rate of total dissipation of the uncontrolled laminar state, respectively), and (b) the E_{uu}–E_{vv} plane. Here, black dashed and cyan solid lines (*Tur* in the figure's legend) indicate uncontrolled and controlled turbulent states, with their means ($\overline{Tur}$ in the figure's legend) represented by open and closed circles. The uncontrolled and controlled equilibrium states are shown by open and closed symbols, respectively. The controlled equilibrium states are presented by averaging over the wall oscillation period.

contrary, the lower-branch solutions show much smaller drag reduction (or even drag increase), and a marginal change of the growth rates of the leading eigenmode is observed, indicating a weak effect of the applied control. These observations are consistent with the reduction in size of the state space region of turbulent state in figure 11.

It is well understood that the uncontrolled turbulent state at $Re = 400$ in the given computational domain is a 'chaotic saddle', which is characterised by the finite lifetime of the chaotic dynamics. The lifetime of the uncontrolled turbulent state also increases very rapidly with the Reynolds number (Eckhardt *et al.* 2007). The state space characteristics discussed in figures 11 and 12 suggest that the effect of the spanwise wall oscillation is similar to that of lowering the Reynolds number, indicating a reduction of turbulence lifetime due to the wall oscillation. To evaluate the turbulence lifetime statistics, we performed groups of 100 controlled and uncontrolled DNS at $Re = 400$. The initial conditions of the simulations were obtained from 100 states computed at a slightly higher Reynolds number, $Re = 415$. The lifetime is evaluated as a probability distribution for the amplitude $A_w^+ = 1.2$ and different oscillation periods $T^+ = 57.2$, 71.5, 85.8, 114.4 and 172. To monitor the lifetime of each simulation, we define a threshold of the turbulent energy fluctuation $E_{vv} + E_{ww} < 10^{-5}$, below which turbulence will decay to laminar flow. The probability for turbulence to live up to a given time t as a function of A_w^+ and T^+ is reported in figure 13. The exponential distribution of the lifetime implies the memoryless nature of the decay process for different initial conditions (see the linear red dashed lines in figure 13), as shown by Eckhardt *et al.* (2007). The lifetime probability decreases with T^+ at $A_w^+ = 1.2$. It is clear that the control tends to relaminarise the flow faster, as the wall oscillation period is increased. Importantly, the exponential lifetime distributions obtained by varying the oscillation parameters suggest that the way that the flow is relaminarised faster by the control is similar to that by reducing the Reynolds number, as the reduction of the lifetime maintaining the memoryless nature has been observed as the effect of the Reynolds number (e.g. Eckhardt *et al.* 2007).

https://doi.org/10.1017/jfm.2022.606 Published online by Cambridge University Press

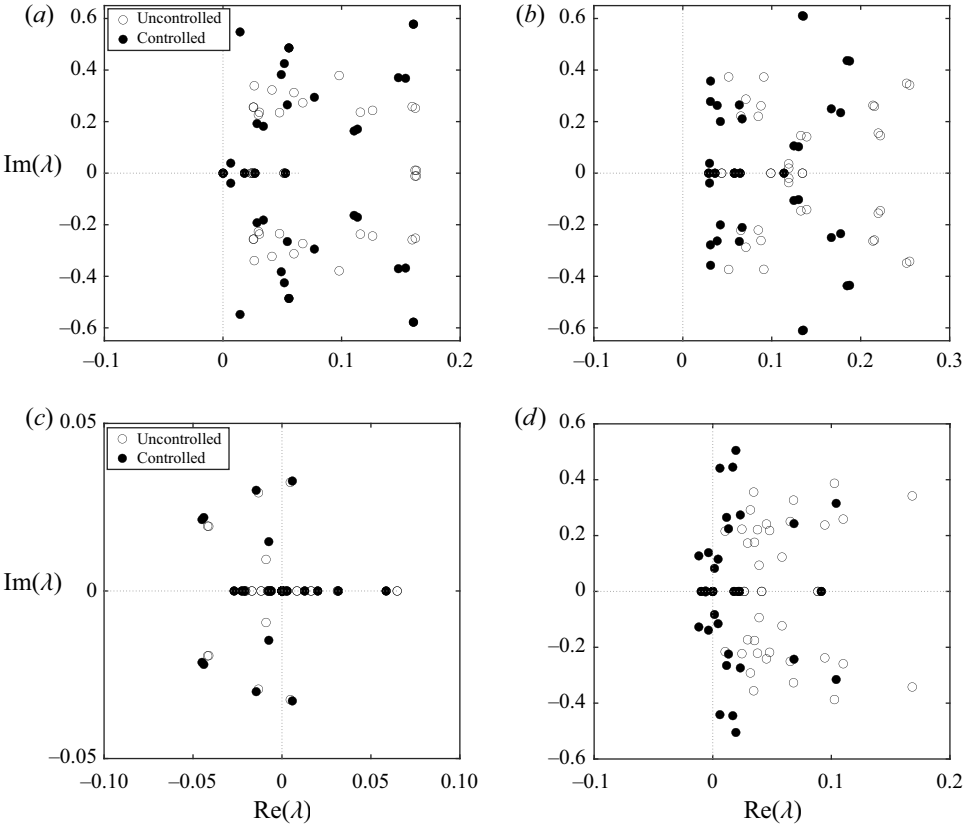


Figure 12. Eigenspectra at $Re = 400$ compared between uncontrolled and controlled ($A_w^+ = 17.7$, $T^+ = 14.3$) states for: (*a*,*b*) EQ4, and (*c*,*d*) EQ7. The lower-branch solutions are shown in (*a*,*c*), and the upper-branch in (*b*,*d*).

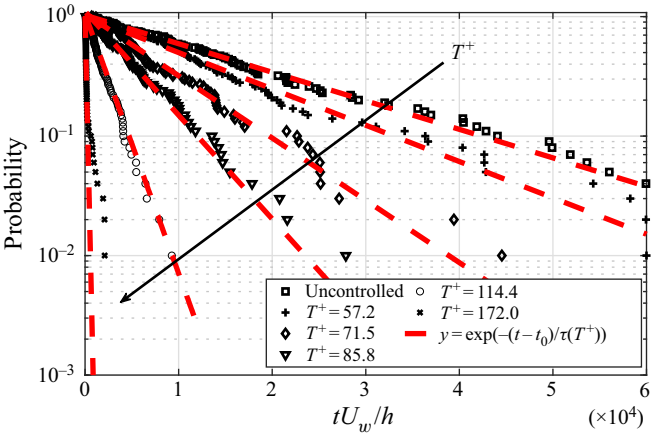


Figure 13. Probability distribution of sustained turbulence lifetime at $Re = 400$ and $A_w^+ = 1.2$ for different spanwise wall oscillation periods T^+. The black arrow indicates the increasing direction of T^+. Here, the red dashed lines indicate a fit obtained using an exponentially decaying function with the characteristic time $\tau(T^+)$ that depends on the oscillation time period.

https://doi.org/10.1017/jfm.2022.606 Published online by Cambridge University Press

3.5. *Stabilisation mechanism of exact coherent states*

Finally, we explore the stabilisation mechanism of the ECS in terms of the self-sustaining process (Hamilton *et al.* 1995). To this end, the velocity fluctuation is decomposed into the streamwise mean and the rest: i.e. $\boldsymbol{u}' = \boldsymbol{u}_1 + \boldsymbol{u}_2$, where $\boldsymbol{u}_1 = \langle \boldsymbol{u}' \rangle_x$. Then $\boldsymbol{u}_1$ describes primarily the streamwise uniform (or elongated) streaks, while $\boldsymbol{u}_2$ depicts the instability wave arising from the streaks and the resulting quasi-streamwise vortices. The equations of motion for $\boldsymbol{u}_1$ and $\boldsymbol{u}_2$ are written as

$$\frac{\partial \boldsymbol{u}_1}{\partial t} + (\boldsymbol{U}\cdot\boldsymbol{\nabla})\boldsymbol{u}_1 + (\boldsymbol{u}_1\cdot\boldsymbol{\nabla})\boldsymbol{U} = -\frac{1}{\rho}\boldsymbol{\nabla} p_1 + \nu\,\nabla^2\boldsymbol{u}_1 - (\boldsymbol{u}_1\cdot\boldsymbol{\nabla})\boldsymbol{u}_1 - \langle(\boldsymbol{u}_2\cdot\boldsymbol{\nabla})\boldsymbol{u}_2\rangle_x + \langle(\boldsymbol{u}\cdot\boldsymbol{\nabla})\boldsymbol{u}\rangle_{x,z}, \tag{3.6a}$$

$$\frac{\partial \boldsymbol{u}_2}{\partial t} + [(\boldsymbol{U}+\boldsymbol{u}_1)\cdot\boldsymbol{\nabla}]\boldsymbol{u}_2 + (\boldsymbol{u}_2\cdot\boldsymbol{\nabla})(\boldsymbol{U}+\boldsymbol{u}_1) = -\frac{1}{\rho}\boldsymbol{\nabla} p_2 + \nabla^2\boldsymbol{u}_2 + \mathcal{N}, \tag{3.6b}$$

with

$$\mathcal{N} = -(\boldsymbol{u}_2\cdot\boldsymbol{\nabla})\boldsymbol{u}_2 + \langle(\boldsymbol{u}_2\cdot\boldsymbol{\nabla})\boldsymbol{u}_2\rangle_x. \tag{3.6c}$$

Now, if we multiply $\boldsymbol{u}_1$ by (3.6*a*) and $\boldsymbol{u}_2$ by (3.6*b*), and integrate over the computational domain Ω and time, the following energy-balance equations are obtained:

$$\underbrace{\frac{1}{V}\int_\Omega -\overline{\langle u_1' v_1'\rangle}_{x,z}\frac{\partial U}{\partial y}\,\mathrm{d}V}_{\mathcal{P}_{uv1}} + \underbrace{\frac{1}{V}\int_\Omega -\overline{\langle v_1' w_1'\rangle}_{x,z}\frac{\partial W}{\partial y}\,\mathrm{d}V}_{\mathcal{P}_{vw1}} = \underbrace{\frac{\nu}{V}\int_\Omega \overline{\langle(\boldsymbol{\nabla}\boldsymbol{u}_1')^2\rangle}_{x,z}\,\mathrm{d}V}_{\mathcal{D}_{\boldsymbol{u}1}}, \tag{3.7a}$$

$$\underbrace{\frac{1}{V}\int_\Omega -\overline{\langle u_2' v_2'\rangle}_{x,z}\frac{\partial U}{\partial y}\,\mathrm{d}V}_{\mathcal{P}_{uv2}} + \underbrace{\frac{1}{V}\int_\Omega -\overline{\langle v_2' w_2'\rangle}_{x,z}\frac{\partial W}{\partial y}\,\mathrm{d}V}_{\mathcal{P}_{vw2}} = \underbrace{\frac{\nu}{V}\int_\Omega \overline{\langle(\boldsymbol{\nabla}\boldsymbol{u}_2')^2\rangle}_{x,z}\,\mathrm{d}V}_{\mathcal{D}_{\boldsymbol{u}2}}, \tag{3.7b}$$

where $\mathcal{P}_{uv1}$ is the time-averaged rate of production by the lift-up effect of streaks, $\mathcal{P}_{uv2}$ is the rate of production by the streak instability and breakdown, $\mathcal{P}_{vw1}$ and $\mathcal{P}_{vw2}$ are the productions of streamwise uniform and non-uniform velocity components by the spanwise mean shear from the wall oscillation, and $\mathcal{D}_{\boldsymbol{u}1}$ and $\mathcal{D}_{\boldsymbol{u}2}$ are the rate of dissipation by streamwise uniform and non-uniform velocity components, respectively.

Table 3 lists the values of the energy production terms defined in (3.7) for the upper-branch equilibrium solutions and DNS with/without some suitable spanwise wall oscillations. For all uncontrolled cases, $\mathcal{P}^+_{uv2}$ is very small compared to $\mathcal{P}^+_{uv1}$, indicating that the key production mechanism lies in the lift-up effect of streaks. When the control is applied, turbulence production of all upper-branch solutions and DNS exhibits a significant reduction. In particular, the reduction in the production appears dominantly in $\mathcal{P}^+_{uv1}$, except for EQ4$_U$, which exhibits a significant reduction in $\mathcal{P}^+_{uv2}$. This suggests that the central mechanism of the stabilisation of the ECS and turbulence is presumably the inhibition of the lift-up effect of streaks by the spanwise wall oscillation, consistent with the observation in § 3.3 where the drag reduction mechanism was proposed in terms of enhanced mixing between low- and high-speed streaky flow regions by the Stokes layer. This also explains why many previous linear analyses (Duque-Daza *et al.* 2012; Moarref & Jovanović 2012; Blesbois *et al.* 2013; Hack & Zaki 2015) have been so successful for a sound description of turbulence suppression and drag reduction by spanwise wall oscillation – one of the main effects that can be quantified by the linear analyses mentioned above is the amplification

https://doi.org/10.1017/jfm.2022.606 Published online by Cambridge University Press

State	A_w^+	T^+	$\mathcal{P}_{uv}^+$	$\mathcal{P}_{uv1}^+$	$\mathcal{P}_{uv2}^+$	$\mathcal{P}_{vw}^+$	$\mathcal{P}_{vw1}^+$	$\mathcal{P}_{vw2}^+$
DNS	0	0	0.08723	0.08139	0.00584	0	0	0
$EQ0_U$	0	0	0.13114	0.11430	0.01682	0	0	0
$EQ1_U$	0	0	0.08964	0.09681	−0.00717	0	0	0
$EQ4_U$	0	0	0.14864	0.08819	0.06045	0	0	0
$EQ7_U$	0	0	0.18393	0.14953	0.03440	0	0	0
DNS	4.7	28.7	0.07949	0.07399	0.00550	−0.00003	−0.00009	0.00006
$EQ0_U$	2.6	166.4	0.08715	0.04786	0.03926	0.00035	−0.00040	0.00075
$EQ1_U$	5.9	14.3	0.06861	0.07473	−0.00613	−0.00002	−0.00001	−0.00001
$EQ4_U$	17.7	14.3	0.09990	0.07411	0.02579	−0.00079	−0.00047	−0.00032
$EQ7_U$	11.8	28.7	0.11355	0.07406	0.03949	−0.00154	−0.00204	0.00050

Table 3. The time-averaged rate of productions of TKE with and without spanwise wall oscillation. For further details, see (3.7).

strength of the streaks by the streamwise vortices (i.e. the lift-up effect). The analysis here also suggests that the nonlinear mechanisms are relatively less important, and they appear to play relatively limited roles in the suppression of turbulence.

4. Conclusion

A set of exact coherent states was investigated subject to spanwise wall oscillation. Generally, the upper branches of the solutions are found to be stabilised significantly by the wall oscillation, whereas the lower branches are affected only modestly. The significantly stabilised upper-branch solutions lead the saddle–node bifurcation point of the solutions to higher Reynolds numbers, although such a trend is reversed at least for EQ0 when $T^+ \gtrsim 100$, consistent with the observation in previous DNS studies. The exact coherent states reproduce the typical streak variation behaviours observed in previous numerical and experimental work, and unveil the rich dynamics of coherent structures under the spanwise wall oscillation. In particular, it was observed that the Stokes layer enhances the fluid mixing between the low- and high-speed streaks, such that the two streaks become more symmetric with each other and subsequently weaken the wall-normal gradient of the streamwise velocity (i.e. skin friction). Visualisation of some physically relevant state portraits shows that the size of the state space supporting the turbulent state is reduced by the spanwise wall oscillation, while the upper-branch equilibrium states become less repelling, with many of their unstable eigenmodes being stabilised. The change in the state space dynamics leads to a significant reduction in lifetime of turbulence. Finally, the main stabilisation mechanism of exact coherent states is the suppression of the lift-up effect, and this explains well why many previous linear analyses have been so successful for stabilisation of turbulence and the resulting drag reduction.

Together with previous studies on exact coherent states under flow controls (Stone *et al.* 2002, 2004; Li *et al.* 2006; Li & Graham 2007; Ibrahim *et al.* 2019; Davis & Park 2020), the present study suggests that the drag reduction mechanism is linked closely to stabilisation of turbulence. Although the controls often have a very modest effect on the lower-branch solutions, they stabilise strongly the upper-branch solutions mainly supporting the turbulent state. This leads to an increase of the critical Reynolds number for the saddle–node bifurcation of the exact coherent states, consistent with the increased

https://doi.org/10.1017/jfm.2022.606 Published online by Cambridge University Press

size of the basin of attraction of the laminar state reported by Rabin *et al.* (2014), and it is associated strongly with reductions in the number of unstable directions and their repelling strength, as well as a reduction in the lifetime of turbulence emerging in the form of a chaotic saddle. In particular, the increase of the Reynolds number of the saddle–node bifurcation point implies that the distance of the upper-branch states and turbulent solution from the lower-branch states and edge state would be reduced by the application of a given control. Therefore, a turbulent state subject to a successful flow control would approach some lower-branch states and the edge state in the state space, explaining the observation by Kushwaha (2017), who reported that turbulence subject to the spanwise wall oscillation appears to stay around a (uncontrolled) lower-branch solution.

Finally, it is worth mentioning that the present study on the exact coherent states under spanwise wall oscillation is valid at low Reynolds numbers. However, given that the near-wall cycle involving the self-sustaining process is known to be statistically and dynamically universal at higher Reynolds numbers (Jiménez & Pinelli 1999; Hwang 2013), the present study would also be relevant to the near-wall region at high Reynolds numbers. Nevertheless, it is important to note that as the Reynolds number is increased, the structures in the logarithmic and outer regions contribute increasingly to the near-wall skin friction (Hwang 2013; de Giovanetti, Hwang & Choi 2016). Therefore, any flow control strategies targeting the near-wall structures are expected to exhibit a performance deterioration on increasing the Reynolds number, and the spanwise wall oscillation for the near-wall structures is not an exception to this (Hurst *et al.* 2014; Gatti & Quadrio 2016; Yao, Chen & Hussain 2019; Marusic *et al.* 2021). In this respect, an interesting variant of the spanwise wall oscillation has been proposed recently by Marusic *et al.* (2021), who obtained a considerable amount of skin-friction reduction with net energy savings by applying a spanwise wall oscillation for large-scale outer structures at high Reynolds numbers. This new finding is certainly beyond the analysis of the present study, although a suitable extension of the dynamical systems approach to such high Reynolds numbers may enable one to analyse the dynamics associated with the drag reduction mechanism (Hwang *et al.* 2016; Yang *et al.* 2019; Yang & Hwang 2019). The effort of extending the concepts from the dynamical systems to high-Reynolds-number turbulence is an issue of ongoing investigation.

Supplementary movies. Supplementary movies are available at https://doi.org/10.1017/jfm.2022.606.

Acknowledgements. We are grateful to Prof M. Graham who shared the PhD thesis of Kushwaha (2017) with us. Q.Y. would like to thank Prof Y.M. Chung for useful discussions.

Funding. Y.B. and Y.H. acknowledge the support of the Engineering and Physical Sciences Research Council (EPSRC; EP/T009365/1) in the UK. Q.Y. acknowledges the Natural Science Foundation of China (92052301; 11802322) and the National Numerical Windtunnel (NNW) project.

Declaration of interests. The authors report no conflict of interest.

Author ORCIDs.
Yacine Bengana https://orcid.org/0000-0001-8993-1714;
Qiang Yang https://orcid.org/0000-0002-1059-2308;
Yongyun Hwang https://orcid.org/0000-0001-8814-0822.

Appendix A. Validation

In this appendix we present the validation of the code used in this study against the literature. We also present the effect of the spatial resolution on the EQ7

https://doi.org/10.1017/jfm.2022.606 Published online by Cambridge University Press

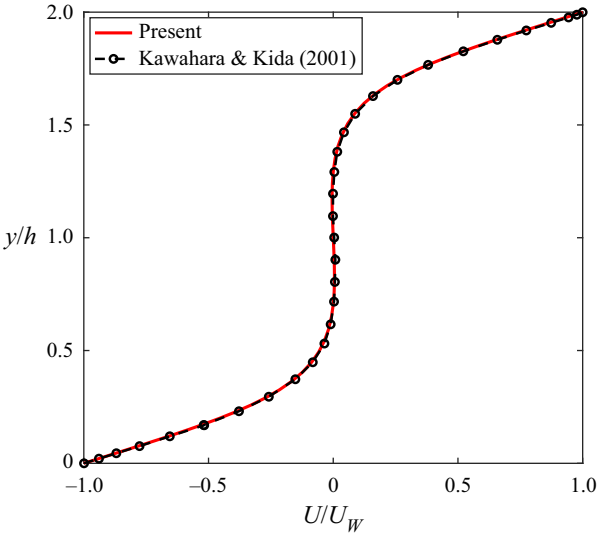


Figure 14. The mean velocity profile of the uncontrolled full DNS simulation at $Re = 400$ with $(N_x, N_y, N_z) = (36, 61, 64)$, compared to that of Kawahara & Kida (2001).

State	Re	A_w^+	T^+	N_x	N_y	N_z	Re_τ
EQ7	802.2	23.6	28.7	32	61	64	49.237
EQ7	802.2	23.6	28.7	32	61	76	49.243
EQ7	802.2	23.6	28.7	32	97	64	49.133
EQ7	802.2	23.6	28.7	48	61	64	49.171

Table 4. Effect of streamwise, spanwise and wall-normal grid resolution on Re_τ at $Re = 802.2$ for EQ7 at $A_w^+ = 23.6$ and $T^+ = 28.7$.

equilibrium solution. Figure 14 shows the mean velocity profile of the uncontrolled DNS simulation at $Re = 400$ compared to that of the classical study of Kawahara & Kida (2001) at the same parameters. We observe that our mean velocity profile matches perfectly that of Kawahara & Kida (2001). Moreover, the discretisation error of the EQ7 equilibrium solution to the grid resolution is less than 0.2 %, as shown in table 4.

Appendix B. Statistics for other exact coherent states

To verify that the statistics observation for EQ0 shown in figure 7 is generic, we show further the r.m.s. profiles for the equilibrium states computed in the domain Ω_{HKW}. Figure 15 shows the r.m.s. velocity profile comparison between the controlled and uncontrolled cases for EQ1, EQ4 and EQ7. Similarly to EQ0 in figure 7, the r.m.s. profiles of the upper-branch solutions with spanwise wall oscillation become closer to those of the lower-branch solutions, which exhibit modest change by the oscillation.

https://doi.org/10.1017/jfm.2022.606 Published online by Cambridge University Press

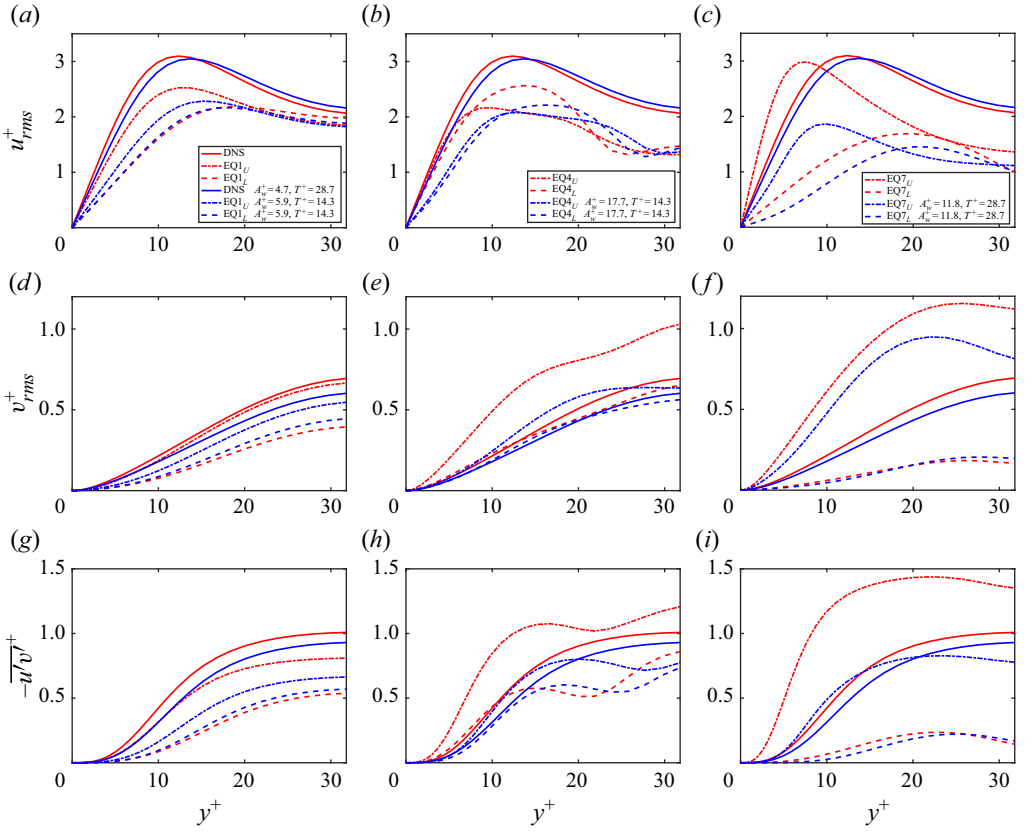


Figure 15. Root-mean-square (r.m.s.) velocity profiles scaled with viscous inner units of the uncontrolled DNS: (*a–c*) u^+_{rms}, (*d–f*) v^+_{rms}, and (*g–i*) $-\overline{u'v'}^+$. The blue and red lines indicate the controlled and uncontrolled cases, respectively. Blue solid lines: fully developed state at $A_w^+ = 4.7$ and $T^+ = 28.7$. Upper branches are shown with dash-dotted lines, and lower branches with dashed lines: (*a*,*d*,*g*) EQ1 with $A_w^+ = 5.9$, $T^+ = 14.3$; (*b*,*e*,*h*) EQ4 with $A_w^+ = 17.7$, $T^+ = 14.3$; (*c*,*f*,*i*) EQ7 with $A_w^+ = 11.8$, $T^+ = 28.7$.

References

Agostini, L. & Leschziner, M. 2021 Statistical analysis of outer large-scale/inner-layer interactions in channel flow subjected to oscillatory drag-reducing wall motion using a multiple-variable joint-probability-density function methodology. *J. Fluid Mech.* **923**, A25.

Agostini, L., Touber, E. & Leschziner, M.A. 2014 Spanwise oscillatory wall motion in channel flow: drag-reduction mechanisms inferred from DNS-predicted phase-wise property variations at $Re_\tau = 1000$. *J. Fluid Mech.* **743**, 606–635.

del Álamo, J.C. & Jiménez, J. 2006 Linear energy amplification in turbulent channels. *J. Fluid Mech.* **559**, 205–213.

Auteri, F., Baron, A., Belan, M., Campanardi, G. & Quadrio, M. 2010 Experimental assessment of drag reduction by traveling waves in a turbulent pipe flow. *Phys. Fluids* **22** (11), 115103.

Baron, A. & Quadrio, M. 1995 Turbulent drag reduction by spanwise wall oscillations. *Appl. Sci. Res.* **55** (4), 311–326.

Bewley, T.R. 2014 *Numerical Renaissance: Simulation, Optimisation and Control*. Renaissance Press.

Bird, J., Santer, M. & Morrison, J.F. 2018 Experimental control of turbulent boundary layers with in-plane travelling waves. *Flow Turbul. Combust.* **100** (4), 1015–1035.

Blesbois, O., Chernyshenko, S.I., Touber, E. & Leschziner, M.A. 2013 Pattern prediction by linear analysis of turbulent flow with drag reduction by wall oscillation. *J. Fluid Mech.* **724**, 607–641.

https://doi.org/10.1017/jfm.2022.606 Published online by Cambridge University Press

BRANDT, L. 2014 The lift-up effect: the linear mechanism behind transition and turbulence in shear flows. *Eur. J. Mech.* B/*Fluids* **47**, 80–96.

BUDANUR, N.B., SHORT, K.Y., FARAZMAND, M., WILLIS, A.P. & CVITANOVIC, P. 2017 Relative periodic orbits form the backbone of turbulent pipe flow. *J. Fluid Mech.* **833**, 274–301.

BUTLER, K.M. & FARRELL, B.F. 1993 Optimal perturbations and streak spacing in wall-bounded turbulent shear flow. *Phys. Fluids* **5**, 774–777.

CASSINELLI, A., DE GIOVANETTI, M. & HWANG, Y. 2017 Streak instability in near-wall turbulence revisited. *J. Turbul.* **18** (5), 443–464.

CHERNYSHENKO, S.I. & BAIG, M.F. 2005 The mechanism of streak formation in near-wall turbulence. *J. Fluid Mech.* **544**, 99–131.

CHOI, H., MOIN, P. & KIM, J. 1993 Direct numerical simulation of turbulent flow over riblets. *J. Fluid Mech.* **255**, 503–539.

CHOI, H., MOIN, P. & KIM, J. 1994 Active turbulence control for drag reduction in wall-bounded flows. *J. Fluid Mech.* **262**, 75–110.

CHOI, J.-I., XU, C.-X. & SUNG, H.J. 2002 Drag reduction by spanwise wall oscillation in wall-bounded turbulent flows. *AIAA J.* **40** (5), 842–850.

CHOI, K.-S. 1989 Near-wall structure of a turbulent boundary layer with riblets. *J. Fluid Mech.* **208**, 417–458.

CHOI, K.-S., DEBISSCHOP, J. & CLAYTON, B.R. 1998 Turbulent boundary-layer control by means of spanwise-wall oscillation. *AIAA J.* **36** (7), 1157–1163.

CHOI, K.-S. & GRAHAM, M. 1998 Drag reduction of turbulent pipe flows by circular-wall oscillation. *Phys. Fluids* **10** (1), 7–9.

CHOI, K.-S., JUKES, T. & WHALLEY, R. 2011 Turbulent boundary-layer control with plasma actuators. *Phil. Trans. R. Soc.* A **369**, 1443–1458.

CHUNG, Y.M., HURST, E. & YANG, Q. 2013 DNS of turbulent drag reduction by spanwise wall forcing: the Reynolds number effect. In *8th International Symposium on Turbulence and Shear Flow Phenomena*, article CON1C.

DAVIS, E.A. & PARK, J.S. 2020 Dynamics of laminar and transitional flows over slip surfaces: effects on the laminar–turbulent separatrix. *J. Fluid Mech.* **894**, A16.

DOOHAN, P., BENGANA, Y., YANG, Q., WILLIS, A.P. & HWANG, Y. 2021 The state space and travelling-wave solutions in two-scale wall-bounded turbulence. *J. Fluid Mech.* (submitted).

DOOHAN, P., WILLIS, A.P. & HWANG, Y. 2019 Shear stress-driven flow: the state space of near-wall turbulence as $Re_\tau \to \infty$. *J. Fluid Mech.* **874**, 606–638.

DUGUET, Y., WILLIS, A.P. & KERSWELL, R.R. 2008 Transition in pipe flow: the saddle structure on the boundary of turbulence. *J. Fluid Mech.* **613**, 255–274.

DUQUE-DAZA, C.A., BAIG, M.F., LOCKERBY, D.A., CHERNYSHENKO, S.I. & DAVIES, C. 2012 Modelling turbulent skin-friction control using linearized Navier–Stokes equations. *J. Fluid Mech.* **702**, 403–414.

ECKHARDT, B., SCHNEIDER, T.M., HOF, B. & WESTERWEEL, J. 2007 Turbulence transition in pipe flow. *Annu. Rev. Fluid Mech.* **39**, 447–468.

ECKHARDT, B. & ZAMMERT, S. 2018 Small scale exact coherent structures at large Reynolds numbers in plane Couette flow. *Nonlinearity* **31** (2), R66–R77.

ELLINGSEN, T. & PALM, E. 1975 Stability of linear flow. *Phys. Fluids* **18** (4), 487–488.

FAISST, H. & ECKHARDT, B. 2003 Travelling waves in pipe flow. *Phys. Rev. Lett.* **91**, 224502.

FUKAGATA, K., IWAMOTO, K. & KASAGI, N. 2002 Contribution of Reynolds stress distribution to the skin friction in wall-bounded flows. *Phys. Fluids* **14** (11), L73–L76.

GARCÍA-MAYORAL, R. & JIMÉNEZ, J. 2011 Drag reduction by riblets. *Phil. Trans. R. Soc.* A **369** (1940), 1412–1427.

GATTI, D., GÜTTLER, A., FROHNAPFEL, B. & TROPEA, C. 2015 Experimental assessment of spanwise-oscillating dielectric electroactive surfaces for turbulent drag reduction in an air channel flow. *Exp. Fluids* **56** (5), 110.

GATTI, D. & QUADRIO, M. 2013 Performance losses of drag-reducing spanwise forcing at moderate values of the Reynolds number. *Phys. Fluids* **25** (12), 125109.

GATTI, D. & QUADRIO, M. 2016 Reynolds-number dependence of turbulent skin-friction drag reduction induced by spanwise forcing. *J. Fluid Mech.* **802**, 553–582.

GIBSON, J.F., HALCROW, J. & CVITANOVIC, P. 2008 Visualizing the geometry of state space in plane Couette flow. *J. Fluid Mech.* **611**, 107–130.

GIBSON, J.F., HALCROW, J. & CVITANOVIC, P. 2009 Equilibrium and traveling-wave solutions of plane Couette flow. *J. Fluid Mech.* **638**, 243–266.

DE GIOVANETTI, M., HWANG, Y. & CHOI, H. 2016 Skin-friction generation by attached eddies in turbulent channel flow. *J. Fluid Mech.* **808**, 511–538.

https://doi.org/10.1017/jfm.2022.606 Published online by Cambridge University Press

GOODMAN, J., HOU, T. & TADMOR, E. 1994 On the stability of the unsmoothed Fourier method for hyperbolic equations. *Numer. Math.* **67** (1), 93–129.
GRAHAM, M.D. & FLORYAN, D. 2021 Exact coherent states and the nonlinear dynamics of wall-bounded turbulent flows. *Annu. Rev. Fluid Mech.* **53**, 227–253.
GUSTAVSSON, L.H. 1991 Energy growth of three-dimensional disturbances in plane Poiseuille flow. *J. Fluid Mech.* **224**, 241–260.
HACK, M.J.P. & ZAKI, T.A. 2015 Modal and non-modal stability of boundary layers forced by spanwise wall oscillations. *J. Fluid Mech.* **778**, 389–427.
HAMILTON, J.M., KIM, J. & WALEFFE, F. 1995 Regeneration mechanisms of near-wall turbulence structures. *J. Fluid Mech.* **287**, 317–348.
HICKS, P.D. & RICCO, P. 2015 Laminar streak growth above a spanwise oscillating wall. *J. Fluid Mech.* **768**, 348–374.
HOF, B., VAN DOORNE, C.W.H., WESTERWEEL, J., NIEUWSTADT, F.T.M., FAISST, H., ECKHARDT, B., WEDIN, H., KERSWELL, R.R. & WALEFFE, F. 2004 Experimental observation of nonlinear travelling waves in turbulent pipe flow. *Science* **1305**, 1594.
HOF, B., DE LOZAR, A., AVILA, M., TU, X. & SCHNEIDER, T.M. 2010 Eliminating turbulence in spatially intermittent flows. *Science* **327**, 1491–1494.
HURST, E., YANG, Q. & CHUNG, Y.M. 2014 The effect of Reynolds number on turbulent drag reduction by streamwise travelling waves. *J. Fluid Mech.* **759**, 28–55.
HWANG, Y. 2013 Near-wall turbulent fluctuations in the absence of wide outer motions. *J. Fluid Mech.* **723**, 264–288.
HWANG, Y. & BENGANA, Y. 2016 Self-sustaining process of minimal attached eddies in turbulent channel flow. *J. Fluid Mech.* **795**, 708–738.
HWANG, Y. & COSSU, C. 2010 Amplification of coherent streaks in the turbulent Couette flow: an input–output analysis at low Reynolds number. *J. Fluid Mech.* **643**, 333–348.
HWANG, Y., WILLIS, A.P. & COSSU, C. 2016 Invariant solutions of minimal large-scale structures in turbulent channel flow for Re_τ up to 1000. *J. Fluid Mech.* **802**, R1.
IBRAHIM, J.I., YANG, Q., DOOHAN, P. & HWANG, Y. 2019 Phase-space dynamics of opposition control in wall-bounded turbulent flows. *J. Fluid Mech.* **861**, 29–54.
ITANO, T. & TOH, S. 2001 The dynamics of bursting process in wall turbulence. *J. Phys. Soc. Japan* **70** (3), 703–716.
JIMÉNEZ, J. & MOIN, P. 1991 The minimal flow unit in near-wall turbulence. *J. Fluid Mech.* **225**, 213–240.
JIMÉNEZ, J. & PINELLI, A. 1999 The autonomous cycle of near-wall turbulence. *J. Fluid Mech.* **389**, 335–359.
JOZSA, T.I. 2019 Analytical solutions of incompressible laminar channel and pipe flows driven by in-plane wall oscillations. *Phys. Fluids* **31** (8), 083605.
JUNG, W.-J., MANGIAVACCHI, N. & AKHAVAN, R. 1992 Suppression of turbulence in wall-bounded flows by high-frequency spanwise oscillations. *Phys. Fluids* A **4** (8), 1605–1607.
KARNIADAKIS, G.E. & CHOI, K. -S. 2003 Mechanisms on transverse motions in turbulent wall flows. *Annu. Rev. Fluid Mech.* **35**, 45–62.
KAWAHARA, G. 2005 Laminarization of minimal plane Couette flow: going beyond the basin of attraction of turbulence. *Phys. Fluids* **17** (4), 041702.
KAWAHARA, G. & KIDA, S. 2001 Periodic motion embedded in plane Couette turbulence: regeneration cycle and burst. *J. Fluid Mech.* **449**, 291–300.
KAWAHARA, G., UHLMANN, M. & VAN VEEN, L. 2012 The significance of simple invariant solutions in turbulent flows. *Annu. Rev. Fluid Mech.* **44**, 203–225.
KERSWELL, R.R. 2005 Recent progress in understanding the transition to turbulence. *Nonlinearity* **18**, R17–R44.
KERSWELL, R.R. & TUTTY, O.R. 2007 Recurrence of travelling waves in transitional pipe flow. *J. Fluid Mech.* **584**, 69–102.
KHAPKO, T., KREILOS, T., SCHLATTER, P., DUGUET, Y., ECKHARDT, B. & HENNINGSON, D.S. 2013 Localized edge states in the asymptotic suction boundary layer. *J. Fluid Mech.* **717**, R6.
KRAVCHENKO, A.G., CHOI, H. & MOIN, P. 1993 On the relation of near-wall streamwise vortices to wall skin friction in turbulent boundary layers. *Phys. Fluids* A **5**, 3307.
KREILOS, T. & ECKHARDT, B. 2012 Periodic orbits near onset of chaos in plane Couette flow. *Chaos* **22** (4), 047505.
KREILOS, T., GIBSON, J.F. & SCHNEIDER, T.M. 2016*a* Localized travelling waves in the asymptotic suction boundary layer. *J. Fluid Mech.* **795**, R3.
KREILOS, T., KHAPKO, T., SCHLATTER, P., DUGUET, Y., HENNINGSON, D.S. & ECKHARDT, B. 2016*b* Bypass transition and spot nucleation in boundary layers. *Phys. Rev. Fluids* **1** (4), 043602.

https://doi.org/10.1017/jfm.2022.606 Published online by Cambridge University Press

KÜHNEN, J., SONG, B., SCARSELLI, D., BUDANUR, N.B., RIEDL, M., WILLIS, A.P., AVILA, M. & HOF, B. 2018 Destabilizing turbulence in pipe flow. *Nat. Phys.* **14** (4), 386–390.
KUSHWAHA, A. 2017 Near-wall turbulence and utilisation of the nonlinear dynamics towards control of turbulent flow. PhD thesis, University of Wisconsin-Madison.
LANDAHL, M.T. 1980 A note on an algebraic instability of inviscid parallel shear flows. *J. Fluid Mech.* **98**, 243–251.
LANGHAM, J., EAVES, T.S. & KERSWELL, R.R. 2020 Stably stratified exact coherent structures in shear flow: the effect of Prandtl number. *J. Fluid Mech.* **882**, A10.
LARDEAU, S. & LESCHZINER, M.A. 2013 The streamwise drag-reduction response of a boundary layer subjected to a sudden imposition of transverse oscillatory wall motion. *Phys. Fluids* **25** (7), 075109.
LEE, J., JELLY, T.O. & ZAKI, T.A. 2015 Effect of Reynolds number on turbulent drag reduction by superhydrophobic surface textures. *Flow Turbul. Combust.* **95**, 277–300.
LESCHZINER, M.A. 2020 Friction-drag reduction by transverse wall motion – a review. *J. Mech.* **36** (5), 649–663.
LESCHZINER, M.A., CHOI, H. & CHOI, K. -S. 2011 Flow-control approaches to drag reduction in aerodynamics: progress and prospects. *Phil. Trans. R. Soc.* A **369** (1940), 1349–1351.
LESSEN, M., SADLER, S.G. & LIU, T.-Y. 1968 Stability of pipe Poiseuille flow. *Phys. Fluids* **11** (7), 1404–1409.
LI, W. & GRAHAM, M.D. 2007 Polymer induced drag reduction in exact coherent structures of plane Poiseuille flow. *Phys. Fluids* **19** (8), 083101.
LI, W., XI, L. & GRAHAM, M.D. 2006 Nonlinear travelling waves as a framework for understanding turbulent drag reduction. *J. Fluid Mech.* **565**, 353–362.
LUSTRO, J.R.T., KAWAHARA, G., VAN VEEN, L., SHIMIZU, M. & KOKUBU, H. 2019 The onset of transient turbulence in minimal plane Couette flow. *J. Fluid Mech.* **862**, R2.
MARENSI, E., DING, Z., WILLIS, A.P. & KERSWELL, R.R. 2020 Designing a minimal baffle to destabilise turbulence in pipe flows. *J. Fluid Mech.* **900**, A31.
MARENSI, E., WILLIS, A.P. & KERSWELL, R.R. 2019 Stabilisation and drag reduction of pipe flows by flattening the base profile. *J. Fluid Mech.* **863**, 850–875.
MARUSIC, I., CHANDRAN, D., ROUHI, A., FU, M.K., WINE, D., HOLLOWAY, B., CHUNG, D. & SMITS, A.J. 2021 An energy-efficient pathway to turbulent drag reduction. *Nat. Commun.* **12** (1), 5805.
MCKEON, B.J. & SHARMA, A.S. 2010 A critical-layer framework for turbulent pipe flow. *J. Fluid Mech.* **658**, 336–382.
MOARREF, R. & JOVANOVIĆ, M.R. 2012 Model-based design of transverse wall oscillations for turbulent drag reduction. *J. Fluid Mech.* **707**, 205–240.
NAGATA, M. 1990 Three-dimensional finite-amplitude solutions in plane Couette flow: bifurcation from infinity. *J. Fluid Mech.* **217**, 519–527.
NAGATA, M. & DEGUCHI, K. 2013 Mirror-symmetric exact coherent states in plane Poiseuille flow. *J. Fluid Mech.* **735**, R4.
PARK, J.S. & GRAHAM, M.D. 2015 Exact coherent states and connections to turbulent dynamics in minimal channel flow. *J. Fluid Mech.* **782**, 430–454.
PUJALS, G., GARCÍA-VILLALBA, M., COSSU, C. & DEPARDON, S. 2009 A note on optimal transient growth in turbulent channel flows. *Phys. Fluids* **21**, 015109.
QUADRIO, M. 2011 Drag reduction in turbulent boundary layers by in-plane wall motion. *Phil. Trans. R. Soc.* A **369** (1940), 1428–1442.
QUADRIO, M. & RICCO, P. 2004 Critical assessment of turbulent drag reduction through spanwise oscillations. *J. Fluid Mech.* **521**, 251–271.
QUADRIO, M., RICCO, P. & VIOTTI, C. 2009 Streamwise-travelling waves of spanwise wall velocity for turbulent drag reduction. *J. Fluid Mech.* **627**, 161–178.
QUADRIO, M. & SIBILLA, S. 2000 Numerical simulation of turbulent flow in a pipe oscillating around its axis. *J. Fluid Mech.* **424**, 217–241.
RABIN, S.M.E., CAULFIELD, C.P. & KERSWELL, R.R. 2014 Designing a more nonlinearly stable laminar flow via boundary manipulation. *J. Fluid Mech.* **738**, R1.
REETZ, F., KREILOS, T. & SCHNEIDER, T.M. 2019 Exact invariant solution reveals the origin of self-organized oblique turbulent–laminar stripes. *Nat. Commun.* **10** (1), 2277.
RICCO, P. 2004 Modification of near-wall turbulence due to spanwise wall oscillations. *J. Turbul.* **5** (1), 024.
RICCO, P., OTTONELLI, C., HASEGAWA, Y. & QUADRIO, M. 2012 Changes in turbulent dissipation in a channel flow with oscillating walls. *J. Fluid Mech.* **700**, 77–104.
RICCO, P. & QUADRIO, M. 2008 Wall-oscillation conditions for drag reduction in turbulent channel flow. *Intl J. Heat Fluid Flow* **29** (4), 891–902.

https://doi.org/10.1017/jfm.2022.606 Published online by Cambridge University Press

RICCO, P., SKOTE, M. & LESCHZINER, M.A. 2021 A review of turbulent skin-friction drag reduction by near-wall transverse forcing. *Prog. Aerosp. Sci.* **123**, 100713.
ROMANOV, V.A. 1973 Stability of plane-parallel Couette flow. *Funct. Anal. Applics.* **7** (2), 137–146.
SCHLICHTING, H. 1979 *Boundary-Layer Theory*. Mc Graw-Hill.
SCHNEIDER, T.M, GIBSON, J.F, LAGHA, M., DE LILLO, F. & ECKHARDT, B. 2008 Laminar–turbulent boundary in plane Couette flow. *Phys. Rev.* E **78** (3), 037301.
SCHOPPA, S. & HUSSAIN, F. 1998 A large-scale control strategy for drag reduction in turbulent boundary layers. *Phys. Fluids* **10**, 1049.
SCHOPPA, W. & HUSSAIN, F. 2002 Coherent structure generation in near-wall turbulence. *J. Fluid Mech.* **453**, 57–108.
SENDSTAD, O. 1992 The near-wall mechanics of three-dimensional turbulent boundary layers. PhD thesis, Stanford University.
SKOTE, M. 2013 Comparison between spatial and temporal wall oscillations in turbulent boundary layer flows. *J. Fluid Mech.* **730**, 273–294.
SKUFCA, J.D., YORKE, J.A. & ECKHARDT, B. 2006 Edge of chaos in a parallel shear flow. *Phys. Rev. Lett.* **96** (17), 174101.
STONE, P.A., ROY, A., LARSON, R.G., WALEFFE, F. & GRAHAM, M.D. 2004 Polymer drag reduction in exact coherent structures of plane shear flow. *Phys. Fluids* **16** (9), 3470–3482.
STONE, P.A., WALEFFE, F. & GRAHAM, M.D. 2002 Toward a structural understanding of turbulent drag reduction: nonlinear coherent states in viscoelastic shear flows. *Phys. Rev. Lett.* **89** (20), 208301.
TOUBER, E. & LESCHZINER, M.A. 2012 Near-wall streak modification by spanwise oscillatory wall motion and drag-reduction mechanisms. *J. Fluid Mech.* **693**, 150–200.
VIOTTI, C., QUADRIO, M. & LUCHINI, P. 2009 Streamwise oscillation of spanwise velocity at the wall of a channel for turbulent drag reduction. *Phys. Fluids* **21**, 115109.
VISWANATH, D. 2007 Recurrent motions within plane Couette turbulence. *J. Fluid Mech.* **580**, 339–358.
WALEFFE, F. 1997 On a self-sustaining process in shear flows. *Phys. Fluids* **9**, 883–900.
WALEFFE, F. 1998 Three-dimensional coherent states in plane shear flows. *Phys. Rev. Lett.* **81**, 4140–4143.
WALEFFE, F. 2001 Exact coherent structures in channel flow. *J. Fluid Mech.* **435**, 93–102.
WALEFFE, F. 2003 Homotopy of exact coherent structures in plane shear flows. *Phys. Fluids* **15**, 1517–1534.
WALSH, M.J. 1983 Riblets as a viscous drag reduction technique. *AIAA J.* **21** (4), 485–486.
WEDIN, H. & KERSWELL, R.R. 2004 Exact coherent structures in pipe flow: travelling wave solutions. *J. Fluid Mech.* **508**, 333–371.
WILLIS, A.P., CVITANOVIĆ, P. & AVILA, M. 2013 Revealing the state space of turbulent pipe flow by symmetry reduction. *J. Fluid Mech.* **721**, 514–540.
WILLIS, A.P., HWANG, Y. & COSSU, C. 2010 Optimally amplified large-scale streaks and drag reduction in the turbulent pipe flow. *Phys. Rev.* E **82**, 036321.
XU, C.-X. & HUANG, W.-X. 2005 Transient response of Reynolds stress transport to spanwise wall oscillation in a turbulent channel flow. *Phys. Fluids* **17** (1), 018101.
XU, J., DONG, S., MAXEY, M.R. & KARNIADAKIS, G.E. 2007 Turbulent drag reduction by constant near-wall forcing. *J. Fluid Mech.* **582**, 79–101.
YAKENO, A., HASEGAWA, Y. & KASAGI, N. 2014 Modification of quasi-streamwise vortical structure in a drag-reduced turbulent channel flow with spanwise wall oscillation. *Phys. Fluids* **26** (8), 085109.
YANG, Q. 2016 Turbulent skin-friction drag reduction control by spanwise motion. PhD thesis, University of Warwick.
YANG, Q. & HWANG, Y. 2019 Modulation of attached exact coherent states under spanwise wall oscillation. In *11th International Symposium on Turbulence and Shear Flow Phenomena*, article 257.
YANG, Q., WILLIS, A.P. & HWANG, Y. 2019 Exact coherent states of attached eddies in channel flow. *J. Fluid Mech.* **862**, 1029–1059.
YAO, J., CHEN, X. & HUSSAIN, F. 2018 Drag control in wall-bounded turbulent flows via spanwise opposed wall-jet forcing. *J. Fluid Mech.* **852**, 678–709.
YAO, J., CHEN, X. & HUSSAIN, F. 2019 Reynolds number effect on drag control via spanwise wall oscillation in turbulent channel flows. *Phys. Fluids* **31** (8), 085108.

https://doi.org/10.1017/jfm.2022.606 Published online by Cambridge University Press